Monthly Notices of the ROYAL ASTRONOMICAL SOCIETY

MNRAS **512,** 4003–4020 (2022) https://doi.org/10.1093/mnras/stac336
Advance Access publication 2022 February 12

Chemistry and physical properties of the born-again planetary nebula HuBi 1

B. Montoro-Molina [1]★ M. A. Guerrero [1] B. Pérez-Díaz [1] J. A. Toalá [2] S. Cazzoli [1] M. M. Miller Bertolami [3,4] and C. Morisset[5]

[1]*Instituto de Astrofísica de Andalucía, IAA-CSIC, Glorieta de la Astronomía S/N, E- Granada, Spain*
[2]*Instituto de Radioastronomía y Astrofísica, UNAM Campus Morelia, Apartado Postal 3-72, 58090 Morelia, Michoacán, Mexico*
[3]*Instituto de Astrofísica de La Plata, UNLP-CONICET, B1900FWA La Plata, Argentina*
[4]*Facultad de Ciencias Astronómicas y Geofísicas, UNLP, B1900 La Plata, Argentina*
[5]*Instituto de Astronomía, Universidad Nacional Autónoma de México, Ensenada, 22860 BC, Mexico*

Accepted 2022 January 31. Received 2022 January 28; in original form 2021 November 19

ABSTRACT

The central star of the planetary nebula (PN) HuBi 1 has been recently proposed to have experienced a very late thermal pulse (VLTP), but the dilution of the emission of the recent ejecta by that of the surrounding H-rich old outer shell has so far hindered confirming its suspected H-poor nature. We present here an analysis of the optical properties of the ejecta in the innermost regions of HuBi 1 using MEGARA high-dispersion integral field and OSIRIS intermediate-dispersion long-slit spectroscopic observations obtained with the 10.4-m Gran Telescopio de Canarias. The unprecedented tomographic capability of MEGARA to resolve structures in velocity space allowed us to disentangle for the first time the Hα and Hβ emission of the recent ejecta from that of the outer shell. The recent ejecta is found to have much higher extinction than the outer shell, implying the presence of large amounts of dust. The spatial distribution of the emission from the ejecta and the locus of key line ratios in diagnostic diagrams probe the shock excitation of the inner ejecta in HuBi 1, in stark contrast with the photoionization nature of the H-rich outer shell. The abundances of the recent ejecta have been computed using the MAPPINGS V code under a shock scenario. They are found to be consistent with a born-again ejection scenario experienced by the progenitor star, which is thus firmly confirmed as a new 'born-again' star.

Key words: stars: evolution – stars: winds, outflows – ISM: jets and outflows – planetary nebulae: general – planetary nebulae: individual (HuBi 1).

1 INTRODUCTION

Planetary nebulae (PNe) are the short-lived descendants of low- and intermediate-mass stars ($1 \lesssim M_{\rm i} \lesssim 8$ M$_\odot$) in their transition from the asymptotic giant branch (AGB) to the white dwarf (WD) phase. At this stage, these stars have completely burnt H and He in their interiors, leaving a $\simeq$0.6 M$_\odot$ C-O core. After ejecting most of their H-rich envelopes, the now post-AGB star evolves increasing its surface temperature at roughly constant luminosity burning the rest of its envelope until H is exhausted. The central star (CSPN) enters then the WD cooling track, irradiating thermal energy, and cooling down.

A selected group of PNe can experience a 'second life'. During the post-AGB evolution, their CSPNe can build up a He mantle, reaching the conditions for a very late thermal pulse (VLTP, Schönberner 1979; Iben et al. 1983), which converts He into C and O and ejects highly processed H-deficient material at high-speeds into the old H-rich PN (Miller-Bertolami et al. 2006). As the stellar envelope expands, it cools dramatically, pushing the CSPN back to lower effective temperatures ($T_{\rm eff}$), first as an H-deficient giant, now as a late C-rich Wolf–Rayet ([WC]) type star. In a sense, the CSPN is born-again. The new PN emerging inside the old PN will be also referred here as a born-again PN.

HuBi 1 (also known as PM 1-188) has been one of the latest PN to be proposed to belong to the class of born-again PNe (Guerrero et al. 2018). This object has been gaining attention over the years, demonstrating to have a unique late evolutionary behaviour. Hu & Bibo (1990) noticed it to be a low-excitation PN whose CSPN, the bright IR source IRAS 17514 − 1555, has a late [WC] spectral type. According to Pollacco & Hill (1994), this PN consists of a faint extended low-density outer shell with typical PN abundances and an unresolved inner shell with apparent bipolar structure.[1] Discrepancies between the observed electron density ($n_{\rm e}$ $\lesssim$1000 cm^{-3}) and that much higher expected for a nebula around a late [WC] CSPN led Peña, Stasińska & Medina (2001) to propose either a born-again scenario for HuBi 1 or the slow evolution of a low-mass AGB star. The chemical abundances derived at that time (Pollacco & Hill 1994; Peña 2005) were somehow similar to that

[1]Pollacco & Hill (1994) also reported an extremely high density for this inner shell, but it resulted from the contamination of the density sensitive [S II] $\lambda\lambda$6716,6731 doublet by stellar C II emission lines.

★ E-mail: borjamm@iaa.es

of typical Galactic PNe, although the bright He I λ5876 emission line suggested a large He/H abundance ratio. On the other hand, the low effective temperature $T_{\rm eff} \simeq 35\,000$ K of the CSPN (Leuenhagen & Hamann 1998) rather supported the latter scenario (Peña 2005).

It has not been until recently that the born-again scenario in HuBi 1 has gained momentum. Guerrero et al. (2018) noticed a decrease in the CSPN brightness ≃10 mag in the last 46 yr that was attributed to a circumstellar veil of C-rich dust suggested by the presence of numerous carbon lines in the optical spectrum of the CSPN (Pollacco & Hill 1994) and by the strong IR emission (Hu & Bibo 1990). Such C-rich material would have been ejected through a VLTP event and, as it expands and cools down, reaches optimal conditions for its condensation on dust grains (e.g. Perea-Calderón et al. 2009).

Guerrero et al. (2018) proposed that the decreasing ionizing flux of the CSPN causes the recombination of the outer shell, whereas the detection of He II emission from the inner shell and its atypical inverted ionization structure, with He II emission embracing the emission of [O III] and [N II], rather suggest it is shock-heated. Indeed, the detection of material expanding up to ≃300 km s^{-1} in the innermost region of HuBi 1 (Rechy-García et al. 2020) lend strong support to the shock excitation of this region by recent ejecta.

The most convincing evidence to fully declare HuBi 1 to be part of the class of born-again PNe would come from the chemical abundances of the recent ejecta, since noticeable abundances discrepancies are expected in a born-again event. H-poor material and enhanced C, N, and O abundances would be present in the most recent ejecta produced by the VLTP (Miller-Bertolami et al. 2006) with the outer nebula exhibiting 'normal' PNe abundances. However, Peña, Hernández-Martínez & Ruiz-Escobedo (2021) have recently reported no abundances differences between the inner and outer shells of HuBi 1, in accordance with previous studies. These results ought to be questioned as they are based on the assumption of the photoionization of the inner shell, which does not seem to be the case given the evidence for shock excitation. Most importantly, since these authors did not remove the contamination of the bright H Balmer emission lines from the outer shell to the inner shell, their analysis of its spectrum can be expected to artificially enhance its H content.

In this paper, we combine optical high-dispersion integral field spectroscopy (IFS) and intermediate-dispersion long-slit spectroscopic observations of HuBi 1 to isolate the emissions of its inner and outer shells in order to determine the H, He, N, and O abundances of the inner shell. The observations and data reduction are presented in Section 2. The data analysis is discussed in Section 3, where two appendices are presented in order (i) to assess the contribution of the emission from the outer shell to the emission of the inner shell, and (ii) to correct the effects of the atmospheric differential chromatic refraction (DCR) that affects the long-slit spectroscopic observations.[2] The results are presented in Section 4, including maps of extinction and electron density of the inner shell, the assessment of the importance of shocks and ultimately the calculation of the chemical abundances. Finally, the discussion and summary are provided in Sections 5 and 6, respectively.

[2]Peña et al. (2021) used the same long-slit spectroscopic data set presented here, but did not apply any correction for atmospheric DCR. The correction of these effects will be shown to be essential for an appropriate determination of the physical properties and chemical abundances of the inner shell of HuBi 1.

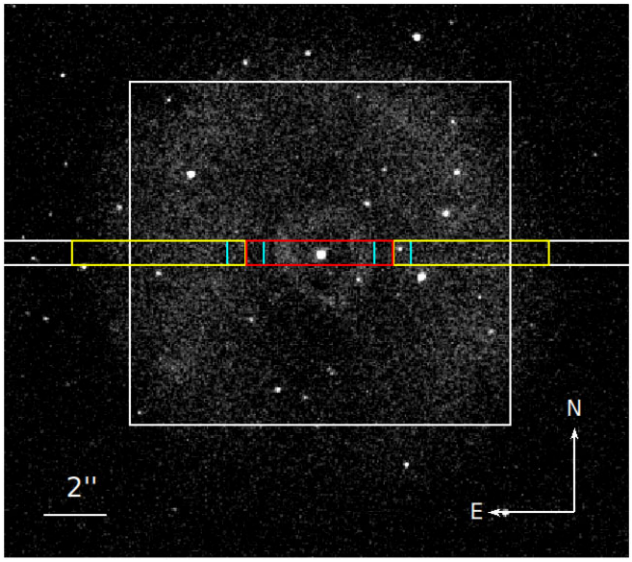

Figure 1. *HST* WFPC2 F656N image of HuBi 1. The positions of the 12.5 × 11.3 arcsec^2 FoV of MEGARA's IFU and the 0.8 arcsec width OSIRIS long-slit are overlaid using white lines lines. This *HST* image reveals clearly the position of background stars included in the apertures of these instruments. The apertures used for extraction of 1D spectra in the OSIRIS data for the inner and outer regions, and from an additional intermediate region are overlaid in red, yellow, and cyan lines, respectively.

2 OBSERVATIONS AND DATA REDUCTION

2.1 GTC MEGARA IFS observations

IFS observations of HuBi 1 were obtained on 2020 August 6 (Program ID GTC96-20A, PI Guerrero) using the Multi-Espectrógrafo en GTC de Alta resolución para Astronomía (MEGARA; Gil de Paz et al. 2018) at the 10.4-m Gran Telescopio Canarias (GTC). The high-resolution (HR) volume-phased holographic (VPH) grism VPH665 and the medium-resolution (MR) grism VPH481 were used.

The observations consisted of three 900 s HR-VPH and six 1000 s MR-VPH exposures obtained under optimal transparency conditions and excellent seeing 0.8 arcsec as measured at the DIMM station. The VPH665 grism provides a spectral dispersion of 0.093 Å pix^{-1} and a full width at half-maximum (FWHM) spectral resolution ≈ 15 km s^{-1}, that is, $R \approx 20\,050$, while the VPH481 grism provides a spectral dispersion of 0.105 Å pix^{-1} and FWHM spectral resolution ≈ 23 km s^{-1}, i. e., $R \approx 13200$. The spectral ranges 4585.7–5025.1 Å and 6405.6–6797.1 Å covered by these two VPHs contain the key emission lines of He II λ4686 Å, Hβ, [O III] λλ4959, 5007 Å, [N II] λλ6548, 6584 Å, Hα, He I λ6678 Å, and [S II] λλ6716, 6730 Å. The integral-field unit (IFU) mode was used. It has 567 hexagonal spaxels with a diameter of 0.62 and a field of view (FoV) of 12.5 × 11.3 arcsec^2, as shown in Fig. 1.

The raw MEGARA data were reduced following the Data Reduction Cookbook (Pascual et al. 2019) using the *megaradrp* v0.10.1 pipeline released on 2019 June 29. This pipeline applies sky and bias subtraction, flat-field correction using halogen internal lamps, wavelength calibration, and spectra tracing and extraction. We note that there is an appreciable illumination pattern making brighter the East and West edges of the FoV, which reduced the cube useful FoV to a region 11.3 × 11.3 arcsec^2 in size. The result is a row-stacked spectrum, which is converted into a 52 × 58 map of 0.″2 arcsec^2 spaxel on spatial dimension and 4300 spaxel on spectral axis using the

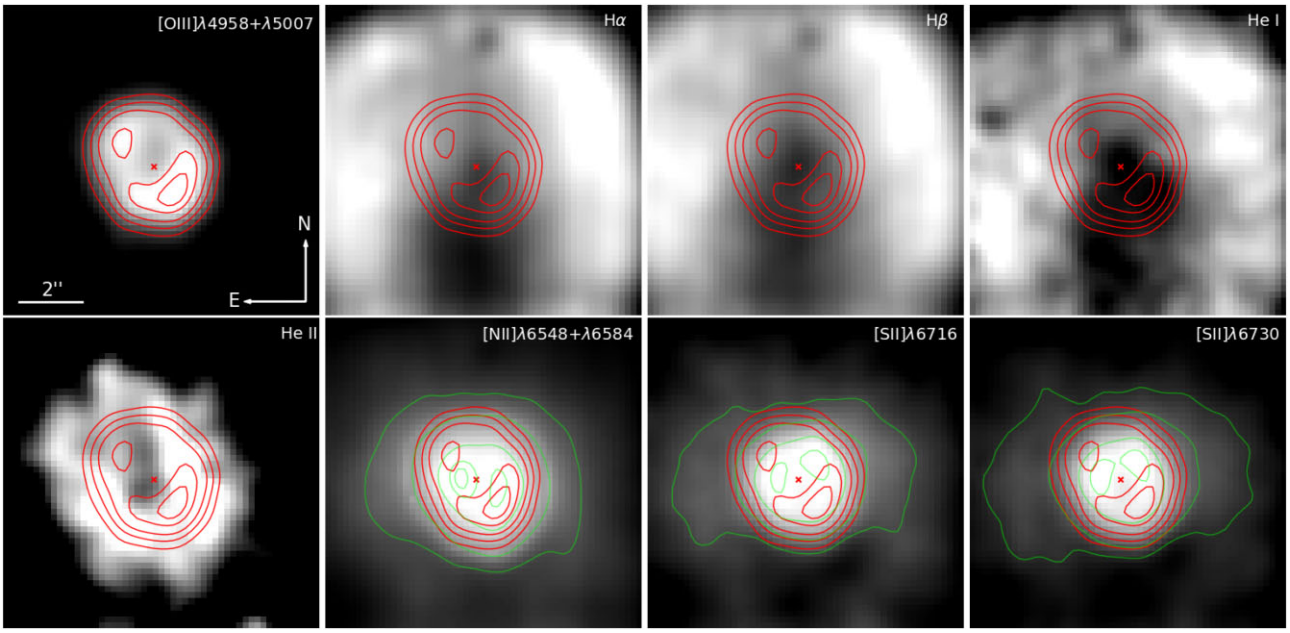

Figure 2. GTC MEGARA maps of HuBi 1 in different emission lines. From the left- to right-hand panels, the panels represent the maps of [O III] λλ4959,5007 Å, Hα, Hβ, and He I λ6678 Å (top panel), and He II λ4686 Å, [N II] λλ6548,6584 Å, [S II] λ6716 Å, and [S II] λ6730 Å (bottom panel). To facilitate the comparison among the different images, red contours extracted from the [O III] image tracing the inner shell are overlaid on all images. Green contours are also overlaid in the [N II] and [S II] images to emphasize the emission from these lines from an intermediate region external to the inner shell. The red contours have been selected at 66, 55, 44, 33, and 22 per cent of the [O III] brightness peak, whereas the green contours have been selected at 75, 70, 55, 25, and 15 per cent of the [N II] brightness peak, and 95, 80, 55, and 40 per cent, of the [S II] brightness peak.

regularization grid task *megararss2cube*. The flux calibrations were performed using observations of the spectrophotometric standard HR 7596 obtained immediately after those of HuBi 1.

2.2 GTC OSIRIS long-slit spectroscopic observations

Intermediate resolution long-slit spectroscopy was acquired on 2018 May 14 (Program ID GTC112-18A, PI Guerrero) with the Optical System for Imaging and low-intermediate-Resolution Integrated Spectroscopy (OSIRIS; Cepa et al. 2000)[3] at the GTC. The observation consisted of 4 exposure of 1575 s on long-slit spectroscopy mode. The R1000B grism was used, providing a spectral dispersion of 2.12 Å pix^{-1} in the spectral range 3630–7500 Å at a spectral resolution $R \approx 1120$. The slit position was placed at a position angle (PA) 90° across the central star (see Fig. 1).

The raw data were bias and sky subtracted and flat-field corrected following standard routines in IRAF (Tody 1993). The wavelength calibration was carried out using Ne and HgAr lamps, whereas the flux calibration was obtained using observations of the spectrophotometric standard star GD 140 obtained in the same night.

The relative flux calibration of the GTC MEGARA and OSIRIS data was checked by comparing the flux of a number of bright emission lines measured from identical spatial apertures in both data sets. These fluxes were found to agree within a few percent.

3 DATA ANALYSIS

The OSIRIS long-slit spectra and MEGARA IFS observations provide a wealth of information on the spatially resolved spectral properties of HuBi 1 that has allowed us to investigate the ionization structure and extract clean spectra of its inner shell. These are described in the next sections.

3.1 The inverted ionization structure of HuBi 1

The final MEGARA data cube allows the extraction of background-subtracted narrow-band images in emission lines of interest, thus providing great versatility to investigate the complex structure of HuBi 1. The data analysis method is as simple as selecting appropriate ranges of spectral channels encompassing an emission line to build a background-subtracted narrow-band image of that emission line. The images of the total integrated flux of key emission lines extracted from the MEGARA data presented in Fig. 2 confirm the remarkable inverted ionization structure of HuBi 1.

The leftmost-top panel of Fig. 2 presents the [O III] emission, which was obtained by adding the [O III] 4959 Å and [O III] 5007-Å emission lines to improve the signal-to-noise ratio (S/N). This emission has a ring-like appearance with an averaged extension of ∼2.5 arcsec in radius. The emission is elongated along the NE direction, with brighter emission at the tips, as shown by the [O III] contours overplotted. The [O III] emission lines uniquely trace the inner region of HuBi 1 and thus [O III] contours will be overplotted on the other key emission line maps of Fig. 2 for comparison.

The images in the Hα, Hβ, and He I 6678-Å emission lines in Fig. 2, on the other hand, trace the outer nebular shell of HuBi 1. Unfortunately, the MEGARA FoV does not cover the full extent of this shell, which has an averaged diameter of ∼15 arcsec. The inner shell of HuBi 1 shown by the red [O III] contours is encompassed by the emission in the Hα, Hβ, and He I lines. It is not possible,

[3] http://www.gtc.iac.es/instruments/osiris/media/OSIRIS-USER-MANUAL_v3_1.pdf

however, to assess whether the inner shell emits in these emission lines or whether the emission detected inside the [O III] contours of the inner shell in these images is rather due to projection effects.

Maps of the low-ionization [N II] and [S II] emission lines are also presented in Fig. 2, where green contours have been used to highlight the distribution and extent of their emission. The bulk of the emission in these low-ionization lines is confined within the red [O III] contours that define the inner shell, with two peaks separated by ∼1.5 arcsec aligned mostly along the east–west direction, i.e. they are clearly misaligned with the peaks in the [O III] image. These images also reveal the presence of an intermediate region[4] spreading out ∼4 arcsec the emission of the inner shell into the outer shell along the east–west direction.

Finally, the leftmost-bottom panel of Fig. 2 shows the spatial distribution of the emission in the line of He II λ4686 Å, the one with the highest ionization potential in the nebular spectrum of HuBi 1. The emission from the inner shell in this emission line is the most extended, with an angular radius of ∼4 × 3 arcsec oriented along a PA similar to that of the emission in the [O III] lines. The He II emission encircles that of the [O III], which surrounds that of the [N II] and [S II] emission lines. The inverted ionization structure of the inner shell of HuBi 1, suggested originally by Guerrero et al. (2018) using 1D line emission spatial profiles, is therefore firmly confirmed in the MEGARA 2D emission maps shown in Fig. 2.

3.2 Dissecting the inner shell of HuBi 1 with MEGARA

The emission of the inner shell of HuBi 1 in the images presented in Fig. 2 would generally include a contribution from the outer shell, as the former is seen through the latter. The emission from the different shells of HuBi 1 can be kinematically separated given their distinct expansion velocities (Guerrero et al. 2018; Rechy-García et al. 2020; Peña et al. 2021) taking advantage of the MEGARA IFS high spectral resolution, although the quality (and reliability) of the kinematic separation of the emission from the two shells in a given emission line would depend certainly on the spatio-kinematic distribution of that line. A detailed description of the different types of lines according to the varying relative contributions of the different structures of HuBi 1 in each emission line is given in Appendix A. These are briefly discussed in the following.

First, the images of the [O III] and He II emission lines can be attributed purely to emission from the inner nebula. We will refer to them as purely internal (PI; see Appendix A) emission lines. On the other hand, the emission of He I arises uniquely from the outer shell and this will accordingly be referred as a purely external (PE; see Appendix A) emission line.

There are then a number of emission lines whose images definitely include emission from both the inner and outer shells. The images of the emission from the [N II] and [S II] lines is mostly dominated by the emission from the inner shell, but there is a non-negligible contribution of emission arising from regions outside the inner shell. These lines are thus referred as internal lines with emission from the external shell (IwE; see Appendix A). We note that the spatial distribution of the outer emission in these lines do not follow the shell-like morphology of the emission in the Hβ, Hα, and He I emission lines, but it is rather spread between the inner and outer shells in a sort of intermediate region. The spatiokinematic distribution of the emission in these lines from this intermediate region does not allow a clear separation from the emission of the inner shell (see discussion section in Toalá et al. 2021b).

Finally, the emission of the Hβ and Hα Balmer lines in the spectral range covered by the MEGARA observations are dominated by the outer shell emission, but the emission from the inner shell can be still kinematically resolved. These lines are referred in Appendix A as external lines with inner emission (EwI). Assessing the specific Hα and Hβ fluxes of the inner and external shells will help us accurately unveil the extinction contribution and abundances for each shell. The emission from the inner shell in these two emission lines will be extracted applying two different methods in the next two subsections.

3.2.1 *High-velocity component isolation in the Hβ and Hα emission*

The inner shell of HuBi 1 can be described as a fast expanding shell-like structure or outflow with expansion velocities up to $\simeq$300 km s^{-1}, well exceeding that of the outer shell $\lesssim$ 50 km s^{-1} (Rechy-García et al. 2020). The high-velocity emission from the inner shell is indeed revealed as red and blue wings in the Hβ and Hα line profiles in the velocity ranges from −14 to +20 km s^{-1} and +108 to +122 km s^{-1} for Hβ, and from −96 to +11 km s^{-1} and +109 to +171 km s^{-1} for Hα. The differences in the velocity ranges of the wings of Hα and Hβ can be attributed to the larger S/N of the former emission line.

The spectral channels of the MEGARA data cube corresponding to the velocity intervals described above have been added to obtain the images of the inner shell in these emission lines shown in the top panels of Fig. 3. The Hα map (top left-hand panel of Fig. 3) is notably less noisy than the Hβ one (top right-hand panel of Fig. 3) due to the better spectral resolution of the HR-VPH and higher S/N of the Hα line. The emission in this Hα map is closely inscribed within the emission of the inner shell represented by the red contours extracted from the [O III] image (leftmost-top panel of Fig. 2). Both the Hα and Hβ maps peak at the Southwest tip of the inner shell, as it does the [O III] emission from the inner shell. Total integrated fluxes of 8.1 × 10^{-15} erg cm^{-2} s^{-1} in Hα and 4.8 × 10^{-16} erg cm^{-2} s^{-1} in Hβ were derived adding the flux in all pixels within a circular area 2.″5 in radius.

3.2.2 *Multi-Gaussian fit to the Hα and Hβ emission lines*

Although the method described in Section 3.2.1 has proven effective to isolate the emissions of the Hα and Hβ lines from the inner shell and to estimate their fluxes, it has some shortcomings. In particular, the selection of the spectral channels (or velocity intervals) mapping the emission of the inner shell is affected by the differing spectral resolution and S/N of the Hβ and Hα lines. As a result, the Hβ map is derived from a velocity interval shorter than that of the Hα map, which may have effects on the Hα/Hβ ratio and on the estimate of the logarithmic extinction coefficient c(Hβ) of the inner shell based on that ratio. Moreover, the channels corresponding to the low-velocity tail of the emission from the inner shell had to be discarded because they were actually dominated by emission from the much brighter outer shell, which may lead to an underestimation of the flux from the inner shell. We remind the reader that one of the main objectives of this work is the determination of the Hα (or Hβ) flux to assess

[4]Here, the emission from the [N II] λ6548 Å and [N II] λ6584 Å emission lines has been added to enhance the weak emission from the intermediate region, whereas the [S II] lines are presented separately because the smaller intensity contrast of the emission from the inner shell and intermediate region allows an easier view of the latter.

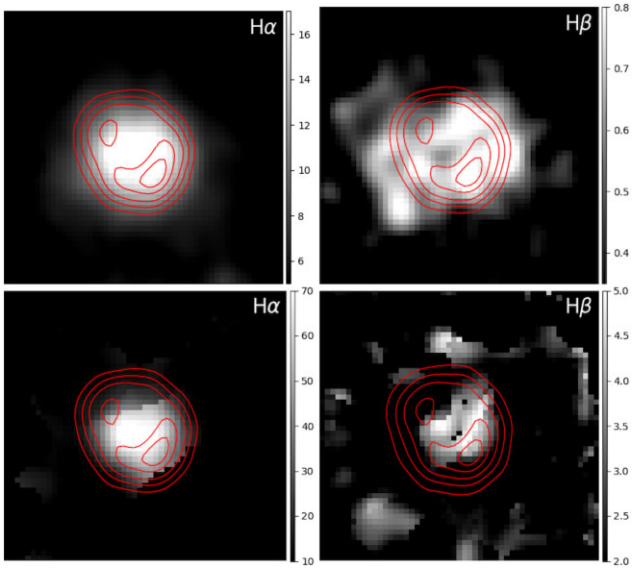

Figure 3. GTC MEGARA Hα and Hβ images of the inner region of HuBi 1 corresponding to the high-velocity components in these emission lines as derived from the isolation of the MEGARA channels within a velocity interval (top panels, see Section 3.2.1) and from the best multi-Gaussian fits (bottom panels, see Section 3.2.2). The extent of the inner shell is shown for comparison using the red contours derived from the [O III] image in Fig. 2. The side scale shows the surface brightness in units of 10^{-17} erg cm^{-2} s^{-1} arcsec^{-2}.

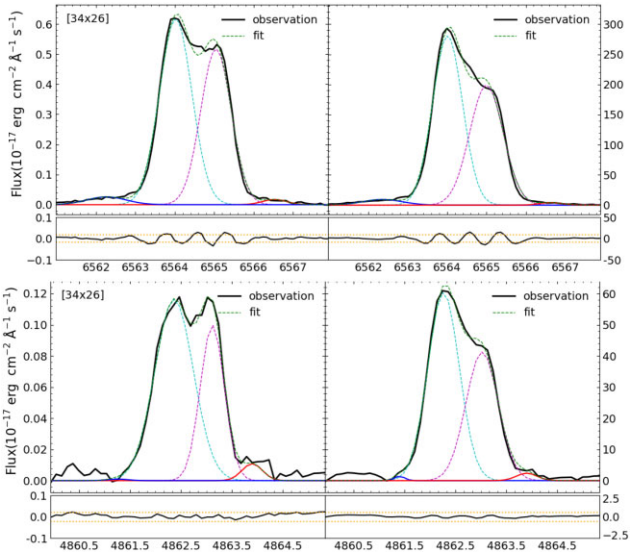

Figure 4. Examples of Hα (top panel) and Hβ (bottom panel) multi-Gaussian fits (left-hand panel) for the spectrum of the pixel (34, 26), which is offset 1.3 arcsec along PA 285° from the centre at pixel (28, 25), and (right-hand panel) for the integrated spectrum of the inner shell, extracted from a circular aperture 2.6 arcsec in radius. The solid black line corresponds to the observed line profile, whereas the green dotted lines represent the multi-Gaussian fit to this profile. The blue, cyan, magenta, and red solid lines correspond to the individual Gaussian components for the fast approaching component of the inner shell, the approaching and receding sides of the outer shell, and the fast receding component of the inner shell, respectively. The bottom panels show the residuals of the fit in solid black lines, whereas the dotted horizontal orange lines correspond to 3σ of the continuum noise derived from representative spectral ranges at both sides of the Hα and Hβ lines, respectively.

whether the chemical abundances of the inner shell of HuBi 1 are consistent with those of a born-again nebula. It is thus critical to obtain reliable values of the Hβ and Hα fluxes for the inner shell.

Therefore, we have explored the determination of these fluxes using multi-Gaussian fits at each pixel on to the inner shell of HuBi 1 to excise the emission of the dominant outer shell from that of the inner shell (see a similar approach in the case of M 2-31, Rechy-García et al. 2021). As described above, this is possible because the inner shell of HuBi 1 has a much larger expansion velocity than the outer shell (Rechy-García et al. 2020). The distinct kinematic behaviour of the inner and outer shells reflects in the spectral profiles of the Hα and Hβ emission lines at the location of the inner shell (approximately the innermost 2.5 arcsec in radius central region), where up to four velocity components can be found; two from the main nebula with slow velocity (one approaching and one moving away) and another two from the inner shell that are detected as high-velocity red and blue wings.

An example of multi-Gaussian fits to the Hα and Hβ emission lines for a pair of pixels projected on to the inner shell[5] is shown in Fig. 4. These are overplotted with the best multi-Gaussian fits revealing the presence of weak red and blue wings corresponding to the inner shell. The small flux contribution from these components might have escaped the previous determination of the Hα and Hβ fluxes. After applying this method to all pixels, the resulting total flux is 1.6×10^{-14} erg cm^{-2} s^{-1} in Hα and 1.1×10^{-15} erg cm^{-2} s^{-1} in Hβ, i.e. about two times the flux derived by the previous method. Maps with the the best multi-Gaussian fits for each pixel are presented in the bottom panels of Fig. 3 for comparison with those obtained in the previous subsection.

[5]The outer shell was also fitted with one, two or up to three components, depending on the spatial location, for continuity with the fit to the inner shell.

3.3 OSIRIS spectra of HuBi 1

The GTC OSIRIS long-slit spectrum, with a broader spectral coverage than the MEGARA data, has been used to extract one-dimensional spectra of the inner and outer shells of HuBi 1. The emission of the inner shell was extracted from a 5 arcsec in length central aperture of the OSIRIS two-dimensional spectrum covering the extent of the [O III] λ5007 emission in the MEGARA maps (the red rectangular aperture in Fig. 1). The emission of the outer region was extracted from two apertures of ∼5 arcsec in length at both sides of the central region (the yellow rectangular apertures in Fig. 1) and then added together. The emission of a transition region between the inner and outer shells was also extracted from two small apertures 1 arcsec in length (the cyan rectangular apertures in Fig. 1) to assess the variation of key emission lines from one region to the other.

The resulting spectra are shown in Fig. 5, with insets to zoom in two spectral regions of interest. These spectra reveal notable spectral variations among the different regions. The [O III] λ5007 emission line is almost as intense as the Hβ line in the inner region (bottom panel of Fig. 5) but, as we moved to more external regions, it fades and mostly disappears (top panel in Fig. 5). On the other hand, the [N II] λ6584 emission line prevails over the Hα line in the inner shell, while in the outer shell their relative importance is reversed (see fig. 8 in Guerrero & Manchado 1996, for a similar case for the born-again PN A 58). These variations in line ratios imply an anomalous ionization structure.

A standard analysis of these spectra involves the measurement of the relative line intensities (e.g. Peña et al. 2021), but it must be

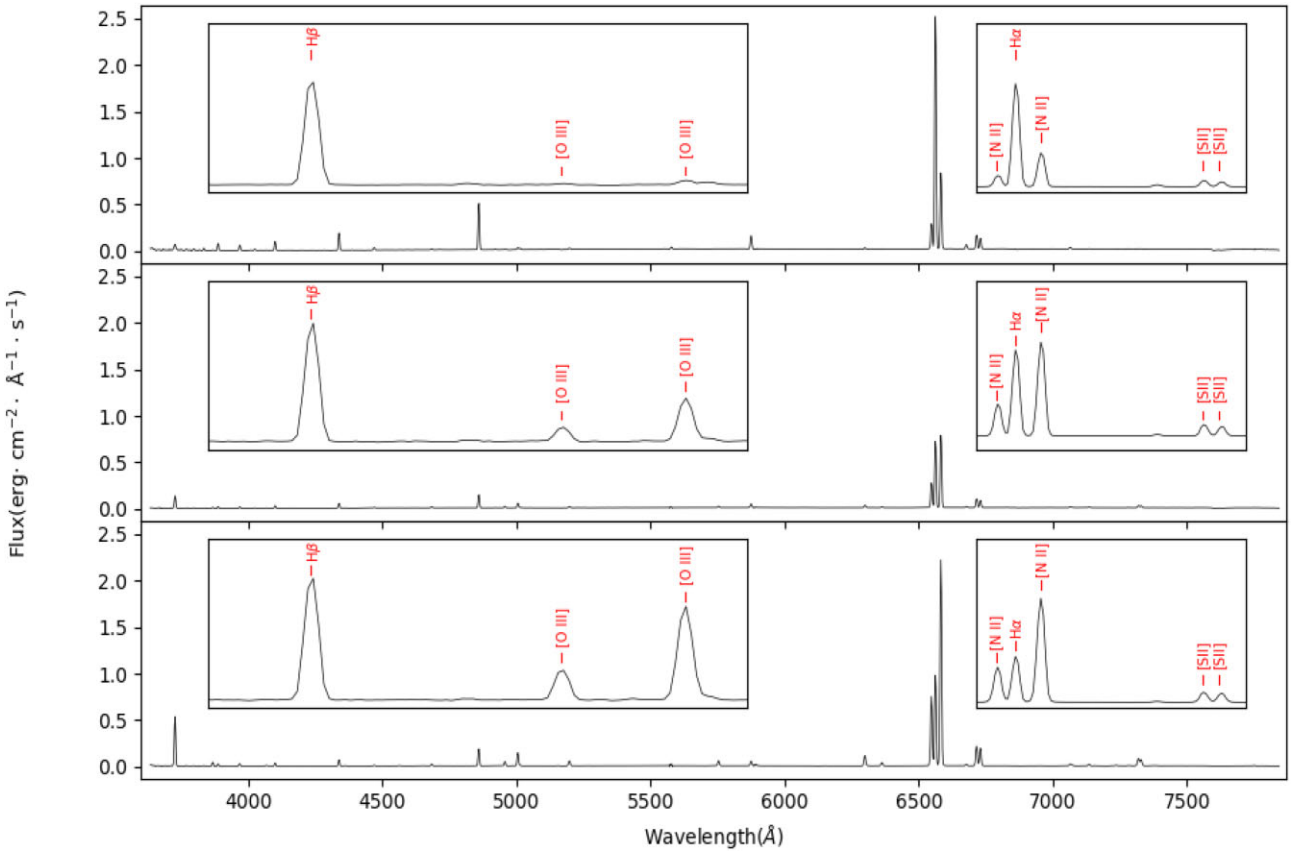

Figure 5. OSIRIS intermediate-dispersion spectra of the outer shell (top panel), intermediate region (middle panel), and inner shell (bottom panel) of HuBi 1 extracted from the yellow, cyan, and red apertures shown in Fig. 1, respectively. Two spectral regions of interest are zoomed to reveal the notable variations in the key emission lines among the different shells.

noted that the GTC OSIRIS spectrum of HuBi 1 was acquired at a low elevation, when the effects of DCR along the parallactic angle cannot be neglected for data obtained over such a broad spectral range (Filippenko 1982). This is a problem particularly serious for these observations, whose slit is almost orthogonal to the parallactic angle. As a result, the apparent position of the slit on the sky for emission lines at different wavelengths will shift noticeably. The details and extent of these effects and a solution using the OSIRIS data in conjunction with the MEGARA data to measure the relative line intensities of the emission lines in the OSIRIS spectra are described in detail in Appendix B.

The observed line flux ratios F with respect to an arbitrary intensity of 100 for the Hβ line together with the Hβ flux for the inner and outer shells of HuBi 1 are presented in Table 1. The features at $\simeq$4566, $\simeq$7236, $\simeq$7289, and $\simeq$7379 Å seem stellar, but none of them except the C II λ7236 line can be unambiguously identified. It shall be noted that the emission arising from the inner shell for a number of emission lines is strongly contaminated by their emission arising from the outer shell. This issue is aggravated for the OSIRIS data, whose low spectral resolution does not allow the spectral split of the emissions from the inner and outer shells. Following the PI, PE, IwE, and EwI classification of the different emission lines according to the relative contribution of the emission of the outer shell to that of the inner shell provided in Section 3.2, the flux of each line has been determined as described in Appendix A.

The intensities of the Hα and Hβ lines have been used to derive the value of the logarithmic extinction coefficient, c(Hβ), for the inner and outer shells of HuBi 1. A recombination Case B was adopted with values for the theoretical I(Hα)/I(Hβ) lines flux ratio (Osterbrock & Ferland 2006) according to the physical conditions of each shell following Ueta & Otsuka (2021)'s prescriptions. Thus a theoretical I(Hα)/I(Hβ) value of 2.74 was adopted for the inner shell, suitable for a value of T_e of 20000 K (close to that reported in Section 4.3), and 3.04 for the outer shell, suitable for a value of T_e of 5000 K (Guerrero et al. 2018; Peña et al. 2021). The values of c(Hβ) derived for the inner and outer shells are 2.16 ± 0.32 and 1.09 ± 0.16, respectively. These have been used in conjunction with the extinction curve of Howarth (1983) to deredden the relative line intensity ratios I also presented in Table 1.

4 RESULTS

The GTC MEGARA, and OSIRIS data presented above allow a detailed spatially resolved spectroscopic investigation of HuBi 1. The results of these analyses are provided in the next sections.

4.1 Extinction maps

The determination of c(Hβ) in the previous section reveals notable higher extinction values for the inner shell. This result is in sharp contrast with the results presented by Pollacco & Hill (1994) and Peña et al. (2021) that did not find spatial variations of the extinction across HuBi 1, with similar values of c(Hβ) for the inner and outer shells. These studies did not accounted for the contamination of the emission of the inner shell by the foreground emission of the outer

Table 1. Relative fluxes and line intensities with respect to Hβ (=100) of the emission lines of HuBi 1 measured from OSIRIS and MEGARA data. Emission lines from OSIRIS for which MEGARA data are available have been replaced by the later. Due to the DCR effects affecting the OSIRIS data, each line of this set is normalized by the Hβ flux computed for the equivalent aperture derived from the MEGARA data (see Appendix A).

Line	Inner shell		Outer shell	
	F	*I*	*F*	*I*
[O II] 3727	2330	8360	27.7	38.3
[Ne III] 3869	197	622	–	–
Hζ + He I 3889	–	–	17.1	28.2
Hϵ + [Ne III] 3969	–	–	14.8	37.8
He I 4026	–	–	4.1	5.0
[S II] 4069	43.4	111	–	–
Hδ 4101	–	–	22.5	34.2
Hγ 4340	–	–	46.7	62.8
[O III] 4363	16.1	30.6	–	–
He I 4471	–	–	8.3	9.9
C I:O II:N II:4562+4570	27.6	39.6	–	–
He II 4686	108	134	–	–
Hβ 4861	100	100	100	100
[O III] 4959	113	101	–	–
[O III] 5007	386	324	–	–
He I 5016	–	–	3.5	2.8
[N I] 5199	114	75.6	4.7	3.2
[N II] 5755	159	60.2	–	–
He I 5876	34.1	20.5	39.7	19.3
[O I] 6300	339	95.5	–	–
[S III] 6312	18.5	4.5	–	–
[O I] 6363	121	28.3	–	–
[N II] 6548	1590	330	50.0	21.1
Hα 6563	1460	274	666	301
[N II] 6584	6820	1390	214	90
He I 6678	–	–	10.0	4.0
[S II] 6717	727	135	42.0	16.7
[S II] 6731	611	112	32.4	12.8
He I 7065	–	–	6.6	2.1
C II 7064 + C I 7066	8.4	1.2	–	–
[Ar III] 7135	80.2	11.1	–	–
C II 7236	33.1	4.3	–	–
C I:O II 7289	25.5	3.2	–	–
[O II] 7320	254	31.6	–	–
[O II] 7330	212	26.2	–	–
N I:O II:7379	22.6	2.7	–	–
log F(Hβ) (erg cm^{-2} s^{-1})	−14.9		−13.3	
c(Hβ)	2.16 ± 0.21		1.09 ± 0.11	

shell, which is particularly severe for the Hα and Hβ Balmer lines used for the determination of c(Hβ).

The tomographic capability of the GTC MEGARA observations highlighted in Sections 3.2.1 and 3.2.2 to isolate the Hα and Hβ emissions of the inner shell from those of the outer shell can be used to investigate the details of the spatial variations of c(Hβ) in HuBi 1. As described in Section 3.2.2, the maps derived using multi-Gaussian fits on a spaxel-by-spaxel basis (lower panels of Fig. 3) are affected by small variations of the fit parameters and are noisier than the maps derived isolating the wings of the high-velocity components (upper panels of Fig. 3). The maps derived using the latter method will be used to produce cleaner c(Hβ) maps, although the velocity range of the Hα and Hβ emission profiles will be restricted to be the same for both lines, as allowed by the S/N of the fainter Hβ line: from −14 to +13 km s^{-1} for the approaching component and from +115 to +122 km s^{-1} for the receding component. In this way, it is warrantied that the Hα to Hβ ratio are derived from similar velocity ranges, although the velocity range for Hα is narrower than that used for the images presented in Fig. 3.

The final extinction maps of the inner and outer shells of HuBi 1 derived from the Hα and Hβ flux map ratios are presented in Fig. 6. These maps indeed confirm that the extinction in the inner shell is larger than that of the outer shell. In order to compare the values in these c(Hβ) maps with the values of c(Hβ) derived in the previous section, average values of c(Hβ) have been derived for the inner and outer shells. For this calculation, pixels with S/N ≤3 have been ignored. In addition, pixels of the inner shell beyond the second contour in Fig. 6 (left-hand panel) were excised because the low Hβ flux, as well as pixels of the outer shell at the corners of the MEGARA IFU FoV where vignetting effects are appreciable. The averaged values of c(Hβ) derived for the inner and outer shells are 2.09 ± 0.21 and 1.14 ± 0.11, respectively, which are consistent with the values derived in the previous section.

The extinction maps presented in Fig. 6 and the averaged values derived above confirm that the extinction in the inner shell is noticeable higher than that of the outer shell. The spatial distribution of the extinction in the inner shell revealed in the left-hand panel of Fig. 6 seems to peak in the innermost regions of the inner shell, at a location between the two peaks of the [O III] map where the CSPN IRAS 17154 − 1555 is located. The extinction in the outer shell is basically flat, but a small increase is found in the regions of the outer shell projected on to the inner shell. This can be attributed to the absorption of the emission from the receding outer shell as it goes through the inner regions of HuBi 1.

Guerrero et al. (2018) attributed the brightness decrease of the CSPN of HuBi 1 of ≃10 mag in the last 50 yr to the ejection of C-rich material that condensed into dust grains and veiled the light from the star rather than to surface temperature of the CSPN. The larger extinction of the inner shell of HuBi 1 found here, in conjunction with the wealth of carbon emission lines detected in its 1991 spectrum (Pollacco & Hill 1994), lends further support to the hypothesis that it contains C-rich material from recent ejecta, while the outer shell is formed by pristine nebular material.

4.2 Diagnostic diagrams

The peculiar ionization structure of HuBi 1, with emission from forbidden lines of [O III] and [N II] dominating the inner shell, but emission from recombination lines of H I and He I in the outer shell, and the presence of He II emission in the inner shell, which cannot be photoionized by its CSPN as its effective temperature is $T_{\rm eff} \approx$ 38 000 K, led Guerrero et al. (2018) to propose that the inner shell is mostly shock-excited. The association of the inner shell of HuBi 1 with a fast expanding (≃300 km s^{-1}) shell-like structure ejected around 200 yrs ago (Rechy-García et al. 2020) provided the means for shock-excitation. More recently, Peña et al. (2021) attributed temporal variations in different line intensity ratios of the inner shell and the increase of the electron temperature in this shell to shock-excitation, but the limitations of their analysis of the spectrum of the inner shell pose questions on their reliability. In particular, the line ratios presented by these authors based on the same GTC OSIRIS data set have not been corrected from DCR effects, which questions the reported line intensity ratio variations (see Appendix B).

Line intensity ratios diagrams have long been used to distinguish between different ionization mechanisms (for instance, the ones defined by Baldwin, Phillips & Terlevich 1981). These diagrams, often used to classify galaxies among AGNs, starburst galaxies or LINERs (Veilleux & Osterbrock 1987; Kewley et al. 2001), can also

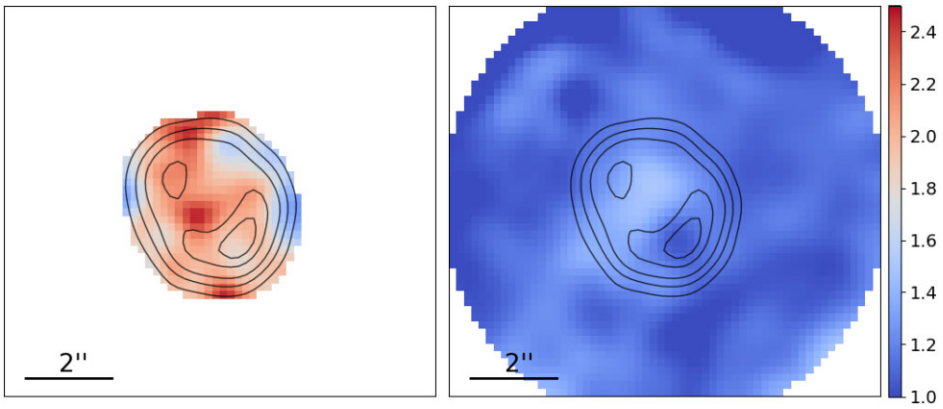

Figure 6. GTC MEGARA maps of the logarithmic extinction coefficient $c(H\beta)$ of the inner (left-hand panel) and outer (right-hand panel) shells of HuBi 1 derived from the Hα to Hβ line flux ratios. Contours of the inner shell derived from the [O III] map are overlaid on the maps. Pixels at the corner regions in the map of the outer shell have been ignored due to vignetting effects.

be applied to PNe. The usual line intensity ratios used for line ratio diagrams are [O III]/Hβ versus [N II]/Hα, [S II]/Hα or [O I]/Hα, but other ratios such as [O III]/Hα versus [S II]/Hα or [N II]/Hα have been used in protoplanetary nebula (pPNe) and PNe and their FLIERs as well (e.g. Raga et al. 2008).

The GTC MEGARA Hβ, Hα, [O III], [N II], and [S II] maps of the inner and outer shells of HuBi 1 have been used to obtain the pixel-by-pixel distributions of the $\log_{10}$([O III]/Hβ) versus $\log_{10}$([N II]/Hα) and $\log_{10}$([S II]/Hα) in the line ratio diagrams presented in Fig. 7. Integrated ratios for the inner and outer shell have been also computed using the GTC OSIRIS long-slit data. The extinction effects in these line ratios is expected to be negligible, given the small wavelength difference, yet the intensity ratios of all points have been corrected using the extinction maps in Fig. 6.

The line ratio diagrams in Fig. 7 clearly reveal that two different mechanism of ionization are present in HuBi 1, being the inner shell dominated by shocks while the outer shell is undoubtedly photoionized. We note that the interpretation of diagnostic diagrams using spatially resolved IFU data can be misleading due to ionization stratification mimicking the behaviour of shock-excited nebulae (Morisset 2018), but this is not the case here as the integrated values of the line ratios obtained from GTC OSIRIS long-slit data share similar loci in these diagrams (Fig. 7). The spread of the data points in these diagrams is notably larger than that in the line ratio diagrams presented by Peña et al. (2021), with values of $\log_{10}$([O III]/Hβ), $\log_{10}$([N II]/Hα) and $\log_{10}$([S II]/Hα) close to unity for the inner shell. These points are located in the region of these line ratio diagrams that can be interpreted as the result of shock-excitation. The spectral coverage of our MEGARA data does not cover the shock-sensitive [O I] λ6300 emission line, but we note that the value of the [O I] λ6300/Hα line intensity ratio derived from the OSIRIS data for the inner shell, $\simeq$0.95, locates it in the region of shock excitation of the $\log_{10}$([O III]λ5007/Hβ) versus $\log_{10}$([O I] λ6300/Hα) line ratio diagram.

The distributions of the points of the outer shell in these line ratio diagrams show a notable spread, with the innermost points closer to the shock ionization region in the line ratio diagrams and the more external points well located in the photoionization region of these diagrams. Such correlation between ionization and radial distance could originate from the regions of diffuse [S II] and [N II] in the so-called intermediate shell, whose ionization may include the effects of shocks. The born-again 3D radiation-hydrodynamic model of HuBi 1 presented by Toalá et al. (2021b) suggests that these structures can appear as the result of the diffusion of turbulence from the ejecta on to the outer shell, which would explain the mixed excitation.

4.3 Physical conditions of the inner shell

We used PyNeb (Luridiana, Morisset & Shaw 2015) to investigate the physical conditions of the inner shell[6] of HuBi 1. The corresponding diagnostic diagrams are shown in Fig. 8, where the shaded areas have been computed assuming a 10 per cent uncertainty for the measured line intensities.

As for the electron density, n_e, the [S II] λ6716 to λ6731 line ratio (the label 'nn' stands for nebular-nebular) draws an area for n_e ranging from a few tens to 1000 cm^{-3}. This value is constrained to 200-600 cm^{-3} in regions where the density diagnostic curve for the [S II] λ6716 to λ6731 line ratio crosses the temperature diagnostic curves.

As for the electron temperature, T_e, the situation is a bit more complex: the [O III] λ4363 to λ5007 line ratio points to T_e between 45 000 and 70 000 K, while the [N II] λ5755 to $\lambda\lambda$6548,6584 line ratio points to much lower values, in the range from 16 000 to 26 000 K. This result can be interpreted as lower ionization N^+ species prevails over higher ionization O^{++} species in regions where the gas have had more time to recombine since the shock passed, and then to cool down. The situation is even more extreme for the [O II] λ3727 to $\lambda\lambda$7320,7330 ratio, which implies a very cold T_e, in the range between 6000 and 9000, and for [S II] $\lambda\lambda$6716,6731 to λ4069 line ratio (labelled 'an' for auroral-nebular), which points to a very high Te, not even shown in the diagram. These results would be hard to reconcile in a photoionized gas, since the O^+, N^+, and S^+ regions are expected to be co-spatial, thus sharing similar physical properties. In the case of shocked regions, however, the steep T_e gradient may cause the emission of a given species to arise from regions at very different temperatures.

The extreme values of T_e derived from the [O II] and [S II] temperature-sensitive line ratios may have an alternative explanation. Both line ratios involve red and blue lines, but in the opposite way, with the nebular [O II] λ3727 line and the auroral [S II] λ4069 line in the blue range. In the next sections, we will see that the blue [O II]

[6]An investigation of the physical conditions of the outer shell cannot be performed because no temperature-sensitive auroral lines are detected in its spectrum.

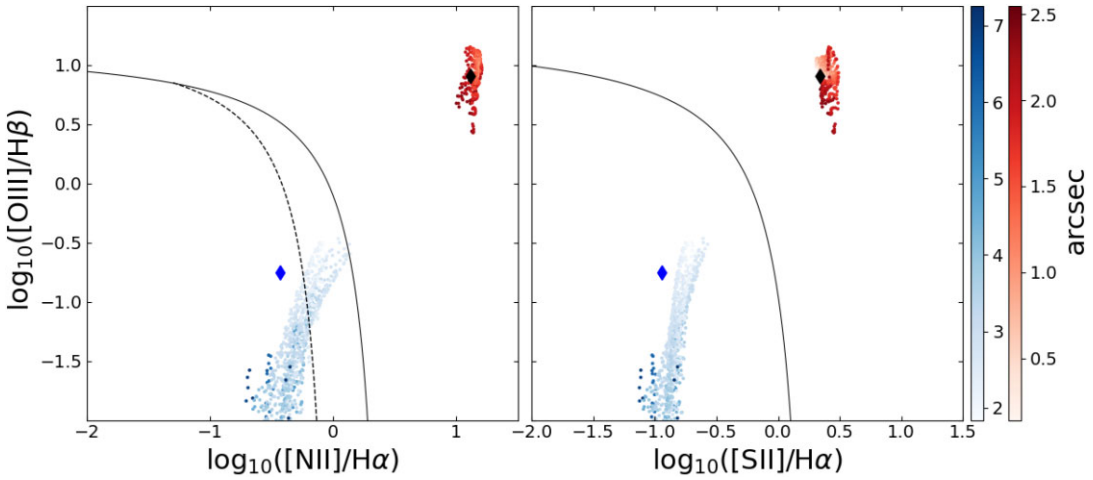

Figure 7. Pixel by pixel distributions of the [O III]λ5007/Hβ, [N II] λ6584/Hα, and [S II]λ(6716 + 6730)/Hα line intensity ratios in the corresponding BPT diagrams for the inner (red points) and outer (blue points) shells of HuBi 1. The blue scale represents the distance of the points of the outer shell to the centre of the nebula from 2.5 to 7.5 arcsec, whereas the red scale shows the distance of the points of the inner shell to the centre of the nebula from 0 to 2.5 arcsec. Data points representative of the inner and outer shells of HuBi 1 derived from the GTC OSIRIS long-slit spectra are shown as cyan and magenta diamonds for the outer and inner shell respectively. The solid and dashed curves correspond to the theoretical models of Kewley et al. (2006) and Kauffmann et al. (2003), respectively.

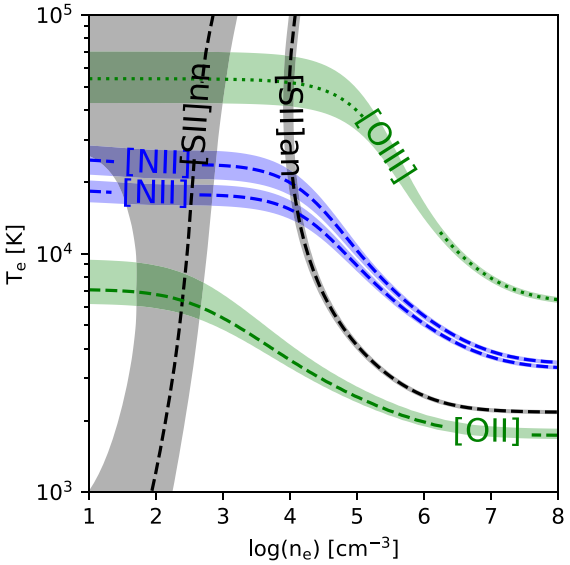

Figure 8. Diagnostic diagrams for the different temperature- and density-sensitive line ratios available in the spectrum of the inner shell of HuBi 1. The shaded areas have been computed assuming a 10 per cent uncertainty for the measured line intensities. The 'an' and 'nn' labels for the [S II] line ratios stand for the auroral λ4069 to nebular λλ6716,6731 and nebular λ6716 to nebular λ6731 line ratios, respectively.

λ3727 and [S II] λ4069 lines, but also the [Ne III] λ3869 line and in a less extent the [O III] λ4363 line are systematically underpredicted by shock models. If the intensity of the [O II] λ3727 line and [S II] λ4069 lines was, indeed, overestimated, it would result in the predicted low T_e for the [O II] line ratio and high T_e for the [S II] line ratio in Fig. 8. Indeed, the value of T_e derived from the [N II] line ratio is the most insensitive to extinction, as it involves lines in the red spectral range.

4.4 Electron density map

The spatial distribution of the nebular density can be derived from the density-sensitive [S II] λ6716, 6731 doublet intensity ratio independently of the excitation mechanism (shocks or photoionization). As described in Section 2 and Appendix A, the [S II] emission lines are classified in Table A1 as IwE, i.e. the emission is mostly attributed to the inner shell with some contribution at systemic velocities arising from the intermediate shell. Their flux maps have thus been computed using a method similar to that applied to the Hα and Hβ lines in Section 3.2.1 with the small differences detailed in Appendix A.

The resulting [S II] λλ6716, 6730 maps are then used to obtain the electron density map using the usual relation between the [S II]λ6716/[S II]λ6730 ratio and n_e (Osterbrock & Ferland 2006) assuming for T_e a value of 30 000 K for the inner shell, within of range of values derived from the [N II] and [O III] temperature-sensitive ratios in the previous section, and 5000 K for the outer shell. Fig. 9 shows the electron density map for all pixels with S/N>3. We obtained averaged densities of $fn_e \approx 500$ cm^{-3} for the inner shell and $n_e \approx 100$ cm^{-3} for the outer shell, the latter in the low-density limit of the density diagnostic provided by the [S II] doublet. The electron density of the outer shell is quite flat, but the inner shell shows two peaks more or less coincident with the [O III] emission peaks.

The electron density of the inner shell agrees with that reported by Guerrero et al. (2018), whereas the extreme high electron density $n_e \simeq 20\,000$ cm^{-3} reported by Pollacco & Hill (1994) can be discarded as those authors did not account for the contamination of the [S II] emission lines by stellar C II lines. Peña et al. (2021) report values for the electron density of the inner and outer shells of HuBi 1 for different epochs between 2000 and 2018 that are suggestive of higher n_e for the inner shell than the outer shell, although the large spread of n_e values makes such result only qualitatively consistent with those obtained here.

4.5 Chemical abundances

Using diagnostic diagrams and the scheme laid out by BPT, we have demonstrated in Section 4.2 that shocks is the main excitation

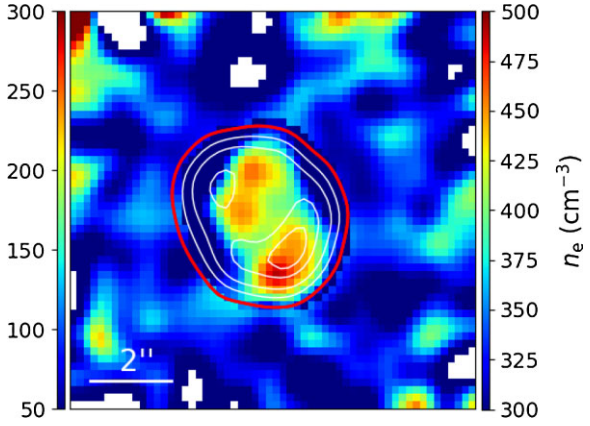

Figure 9. Electron density n_e map of HuBi 1 derived from the [S II] λ6716 to [S II] λ6730 line intensity ratio. The contours of the emission in the [O III] λ5007 line showing the extent of the inner shell are overlaid. The most extended red contour separates the inner and outer shells of HuBi 1. Their densities n_e were computed assuming an electron temperature of 30 000 K for the former (right colorbar) and 5000 K for the latter (left colorbar).

mechanism of the inner shell of HuBi 1. Indeed, the high values of the auroral-to-nebular line ratios [O III] λ4363 Å/[O III] λ5007 Å ∼ 0.09 and [N II] λ5755 Å/[N II] λ6584 Å ∼0.33 are also clear indicators of shocks (Dopita 1977). Since shock excitation has to be taken into account for abundances determination in the inner shell of HuBi 1, we computed those making use of the MAPPINGS V code (Sutherland et al. 2018). Details of the code can be found in Appendix C.

For our modelling, we consider shocks as the only source of ionization in the inner shell as the large extinction towards the CSPN basically absorbs all its UV emission. We ran a number of models taking into account the emission from both the shock and its precursor (Allen et al. 2008; Sutherland & Dopita 2017). According to analyses of spectroscopic observations of the outer shell of HuBi 1 (e.g. Guerrero et al. 2018), shocks in these simulations are assumed to propagate into a fully ionised medium (i.e. $H/H^+ = He/He^+ = 1$) with a pre-shock temperature of 10^4 K.

We start by fixing the values of the shock velocity v_s at 80 km s^{-1} as smaller velocities can be precluded (Rechy-García et al. 2020), the pre-shock density n at 1 cm^{-3} (similar to that found for non-fully radiative young shocks by Dopita et al. 2018), and the strength of the magnetic field B at 1 μG. The latter is low for a PN (Rodríguez et al. 2017), but plausible if we assume that magnetic field scales with density $B \propto n^{1/2}$ as proposed by Cox (2005) for average interstellar medium properties.

We then ran a number of MAPPINGS V models varying the O and N abundances, keeping the He abundance at 12+log$_{10}$(He/H)=13.0 and scaling the abundances of the other heavy elements with those of O according to the Solar abundances (Asplund et al. 2009). The MAPPINGS V models studying the variations of the O and N abundances are presented in Table C1 of Appendix C, where the model line emission strengths are compared with those observed reported in Table 1 to determine the best values for the O and N abundances. The emission line ratio [O III] λ4363 Å/[O III] λ5007 Å, which is particularly sensitive to the shock conditions (Dopita 1977), is used as a main indicator, but the intensities of the [O III], [O II], and [N II] emission lines are also considered

The N/H abundances were first fixed to their Solar values and the O/H abundances allowed to vary (Columns 3–7 of Table C1). It can be seen there that, although O abundances below 12 + log$_{10}$(O/H) < 9.8 reproduce best the auroral-to-nebular [O III] ratio, they clearly underestimate the flux of all O emission lines. Higher O abundances tend to overestimate the [O III] emission lines and predict auroral-to-nebular [O III] ratios much smaller than observed. The model with 12 + log$_{10}$(O/H) = 9.8 ± 0.1, which best reproduces most of the [O III] emission lines, is adopted as best fit model. The O/H abundances were then fixed to this value and the N/H abundances allowed to vary (columns 8 to 12 of Table C1). As for the O abundances, the intensity of the N lines require abundances two orders of magnitudes higher than Solar values, with the best fit achieved at 12 + log$_{10}$(N/H) = 9.9 ± 0.10.

We tried then to assess the He abundance that best reproduces the intensity of the He recombination lines. Table C2 shows that predicted intensity of the He recombination lines scales with the He abundance, although it also has noticeable effects in important collisional lines, such as [N II] λ6584, implying variations at factors of about one half in the N abundances anticorrelated with those of He. On the other hand, the intensity of the O lines and thus their abundances are quite insensitive to variations in the He abundances. We varied the He abundance around a value of 12 + log$_{10}$(He/H) = 13, but the He II λ4686 line was always underestimated, whereas the He I λ5876 line was clearly overestimated. A value of 12 + log$_{10}$(He/H) = 13.00 ± 0.15 was selected as a best compromise.

Finally, we investigated whether the adopted pre-shock density and shock velocity may explain the discrepancies found in some emission line ratios for our fixed set of chemical abundances. In Table C3 we show that increasing the shock velocity v_s from 100 to 200 km s^{-1} tend to decrease all emission line ratios with respect to the [O III] emission lines. Therefore, we conclude that a shock velocity v_s of 80 km s^{-1} is the best choice in agreement with Guerrero et al. (2018). Similarly, we show in Table C4 that increasing the pre-shock density makes closer the estimation of the [O III] ratio to the observed one, but other important emission lines as the [S II] doublet, [O II] and [N II] lines are not well reproduced. Lower densities lead to lower [O III] λ4363/[O III] λ5007 ratios, making them differ more notably from the observed one. Therefore, the best models are adopted to have a pre-density n_{pre} of 1 cm^{-3}.

We list in Table 2 the parameters of our preferred model to reproduce the shock-excited spectrum of the inner shell of HuBi 1. We note that the C abundances in this table are scaled from the O abundances assuming a Solar C/O ratio of ∼0.55 (Asplund et al. 2009), as the available line ratios do not provide a suitable constraint to the C abundances. The [O III] and [N II] lines are fairly well described by this model, with the most notable discrepancies for the He I λ5876 and [O II] λ3727 emission lines. These discrepancies will be discussed in further details in the next section.

5 DISCUSSION

HuBi 1, the inside-out PN, has proven to be a remarkable object, with extreme changes recorded in the past decades (e.g. Guerrero et al. 2018; Peña et al. 2021). Similar variations in human timescales have also been reported for the two youngest born-again PNe identified thus far, namely the Sakurai's Object and A 58, also known as Nova Aql 1919 (see Clayton et al. 2013; Evans et al. 2020, and references therein), as well as for the LTP star SAO 244567 and the nebula around it (Reindl et al. 2017; Balick, Guerrero & Ramos-Larios 2021). Indeed, the dramatic decline in brightness of the CSPN of HuBi 1 by ≃10 mag in ∼50 yr and the strong IR emission and the profusion of C emission lines from the innermost regions detected in the oldest available spectra (Pollacco & Hill 1994) are suggestive of the ejection of highly enriched material that had

Table 2. MAPPINGS V model considered to reproduce the emission from the inner shell in HuBi 1. The emission lines are referred to $I(H\beta)$=100.

Parameter	Preshock	Postshock
Density (n)[cm^{-3}]	1	3.7
Electronic Density (n_e)[cm^{-3}]	5.8	21.4
Temperature (T)[K]	30000	380000
Magnetic field (B)[μG]	1	3.7
Chemical abundances		12+log$_{10}$(X/H)
H		12.00
He		13.00 ± 0.15
C		9.53
N		9.90 ± 0.10
O		9.80 ± 0.10
Ne		9.03
Line	Observation	Model
[O II] 3727	8360	571.2
[Ne III] 3869	622	54.9
[S II] 4069	111	14.2
[O III] 4363	30.6	25.0
He II 4686	134	66.8
[O II] 4959	101	129.2
[O III] 5007	324	373.4
[N II] 5199	75.6	119.3
[N II] 5755	60.2	66.3
He I 5876	<20.5	336.7
[O I] 6300	95.5	30.4
[S III] 6312	4.5	5.3
[O III]6363	28.3	9.7
[N II] 6548	330	552.2
Hα	274	407.4
[N II] 6584	1390	1624
[S II] 6717	135	104.0
[S II] 6731	112	115.0
[Ar III]	11.1	7.8
[O II] 7320	31.6	43.1
[O II] 7330	26.2	34.8

resulted in the sudden formation of large amounts of dust, well in agreement with a born-again scenario. If this were the case, there are a number of predictions that can be uniquely tested using the unequalled capabilities of MEGARA at the GTC to disentangle the inner shell emission from that corresponding to the outer H-rich PN.

Since VLTP events result in the production of large amounts of dust, one basic expectation would be that the inner shell of HuBi 1 should be more extincted than the outer shell. We have for the first time obtained clean extinction maps of the inner and outer shells by dissecting the different contributions of their emission to the H Balmer lines. These unpolluted extinction maps confirm that the inner shell exhibits larger $c(H\beta)$ values than the outer nebula, in contrast with the similar values for both shells reported in previous works (e.g. Peña 2005; Peña et al. 2021). Incidentally, these extinction maps allow us the proper reddening correction of the spectra extracted for the inner and outer shells using the appropriate value of $c(H\beta)$ for each of them.

After experiencing a VLTP event, the CSPN is expected to go back for a short period of time to the locus of the H-R diagram occupied by AGB stars, reducing considerably its effective temperature and thus its ionization photon flux. As a result, photoionization cannot be the main excitation mechanism of the emission arising from the innermost regions of young born-again PNe. Combining MEGARA and OSIRIS data sets, we have obtained reddening-corrected [O III]/Hβ, [N II]/Hα and [S II]/Hα line ratios that have been used to produce standard diagnostic diagrams. The position in these diagrams of data points from the inner shell undoubtedly demonstrate that the main emission mechanism in the inner shell of HuBi 1 is shocks, confirming the original proposition explored by Guerrero et al. (2018).

The most critical test of the born-again nature for the inner shell of HuBi 1 would be a H-poor abundance. We have computed those from the line ratios measured in the MEGARA and OSIRIS data sets using the MAPPINGS V code to conform to the shock-excitation of this region. The best-fitting model (Table 2) is capable to reproduce most of the emission lines detected in our spectra, although the strength of the [O II] λ3727 doublet is notoriously underestimated, whereas those of the He II λ4686 and He I λ5876 emission lines cannot be simultaneously matched. The significant differences between the observed and predicted intensities of the [O II] λ3727 and [O II] λλ7320,7330 emission lines may reveal the complexity of the physical conditions and possibly varying optical depth of the O^+-emitting region. Alternatively, these discrepancies can be partially attributed to the effects of the relatively small photoionization produced by the cool CSPN of HuBi 1 (T_{eff} ≈35–38 kK; Leuenhagen & Hamann 1998; Guerrero et al. 2018), which would raise the emissivity of the [O II] λ3727 doublet and He I λ5876 emission line. More likely there is an over-correction of the extinction of the intensity of the emission lines in the blue end of the spectrum due either to spatially varying absorption or to the use of a generic extinction curve of the interstellar medium, but probably not suitable for the peculiar chemical abundances of the ejecta. Section 4.3 already noted the discrepancies between the electron temperature derived from line ratios involving [O II] and [S II] 'blue' and 'red' lines. Indeed, the shock models here presented does not only underestimate the 'blue' [O II] λ3727 and [S II] λ4069 lines, but also the [Ne III] λ3869 emission line.

The best-fitting model in Table 2 implies the notable hydrogen deficiency in the innermost ejecta of HuBi 1, with He/H ≃10, O/H ≃0.006, and N/H ≃0.008, well above those typical for PNe. These results are in sharp contrast with those recently presented by Peña et al. (2021), who claimed that the chemical composition of the inner and outer shells of HuBi 1 were similar among them and typical of PNe. We note, however, a number of flaws in the analysis presented by Peña et al. (2021) (1) the extinction-correction of the outer shell was applied to the inner shell of HuBi 1, which is inadequate and result in the incorrect determination of the physical conditions of the inner shell, (2) the notable DCR effects in the same OSIRIS long-slit spectra presented here (see Appendix A) were not corrected, (3) photoionization was assumed as the excitation mechanism for the calculation of the inner shell chemical abundances, although they had proven the prevalence of shocks as the main excitation mechanism, and (4) more importantly, the dominant contamination of the outer shell to the Hβ and Hα emission from the inner shell was not subtracted, artificially enhancing the hydrogen content of the inner shell.

The abundances by number obtained in our analysis considering shocks are in excellent agreement with the abundances determined from collisionally excited emission lines (CELs) from the H-poor knots of born-again PNe (Jacoby & Ford 1983; Manchado, Pottasch & Mampaso 1988; Guerrero & Manchado 1996; Wesson, Liu & Barlow 2003; Wesson et al. 2008). Our He/H abundance of 10 is as well in the same range from 3.2 to 11.7 to that obtained for A 30 and A 58 (see table 7 in Wesson et al. 2008). It can thus be concluded that the chemical abundances of the inner shell of HuBi 1 are consistent with the H-poor nature of a born-again scenario.

The chemical abundances of HuBi 1, as those derived for other born-again PNe using CELs, are far from the theoretical expectations from born-again scenarios (e.g. Miller-Bertolami et al. 2006). It is well- known that observed chemical abundances in born-again PNe only become consistent with those theoretically predicted when they are computed using optical recombination lines (ORLs), as the abundances discrepancy factor (ADF), i.e. the ratio between the chemical abundances derived from ORLs and CELs, is extremely high among born-again PNe, with values up to 700 for A 30 (Wesson et al. 2003) and $\simeq$90 for A 58 (Wesson et al. 2008). For comparison, the average ADF[7] Unfortunately, the ORLs needed for the determination of the ADF in HuBi 1 are not available in its spectrum. If an ADF of 100 were adopted, which seems reasonable for born-again PNe, total 'ADF-corrected' abundances by mass of 0.01, 0.58, 0.06, 0.16, 0.15, and 0.04 for H, He, C, N, O, and Ne, respectively, would be obtained.

These 'ADF-corrected' chemical abundances are in the range of the theoretical expectations from born-again scenarios considered above (Miller-Bertolami et al. 2006), but for the N/O ratio close to unity, which seems otherwise typical of nova events (see Lau, De Marco & Liu 2011). This scenario, however, is unlikely, since the slowest novae have velocities $\sim$300−700 km s^{-1} (see,e.g. Santamaría et al. 2020, and references therein), whereas the bulk of material of the hydrogen-poor ejecta of HuBi 1 expands at 80–100 km s^{-1}.

The details of these 'ADF-corrected' abundances do not completely agree with those estimated for the CSPN of HuBi 1 using non-local thermodynamic equilibrium atmosphere models (Leuenhagen & Hamann 1998; Guerrero et al. 2018): the nebular abundances by mass of 0.58 for He and 0.15 for O differ from the stellar values of 0.33 and 0.10, respectively, the nebular N/O ratio is about 10 times larger than the stellar N/O ratio (0.1), and the nebular C abundances are about 8 times smaller than the stellar ones (0.5). On the other hand, the stellar abundances are perfectly matched by the theoretical predictions (Guerrero et al. 2018). We suspect that the differences between the 'ADF-corrected' abundances of HuBi 1 and the stellar abundances and theoretical predictions arise from a notable underestimation of the C abundances and in a minor degree of the O abundances. The C and Ne abundances obtained with our shock model have been estimated using their Solar ratios with respect to the O abundances, but the wealth of C II and C III lines detected by Pollacco & Hill (1994) point to a significant overabundance of C. Moreover, large amounts of C are to be trapped into C-rich dust such as amorphous carbon species as shown in the born-again PNe A 30 and A 78 (Toalá et al. 2021a). In addition, C and O atoms might be trapped into CO molecules, which in the case of the born-again PN A 58 amount to a mass $\simeq 10^{-5}$ M$_\odot$ (Tafoya et al. 2022). If those effects were to be taken into account, the C fraction by mass would increase notably, reducing that of the other elements, and the N/O ratio would be reduced. The total abundances by mass of He, C, N, and O would then become consistent with those of 0.33, 0.5, 0.01, and 0.10, respectively, estimated for the CSPN (Guerrero et al. 2018). The case of the C abundances of the born-again ejecta of HuBi 1 will be addressed in a subsequent paper (Rodríguez-González et al., in prep.) using IR observations to obtain a coherent set of chemical abundances of H, He, C, N, and O (see Toalá et al. 2021a). Future studies that simultaneously model the gas, dust and molecules of born-again PNe will help strengthen our understanding of the evolutionary sequences of the progenitors of such unique objects.

[7]See https://www.nebulousresearch.org/adfs for the most up to date list of ADFs in PNe. of hydrogen-rich PNe is $\simeq$2 (Wesson et al. 2018).

6 CONCLUSIONS

We have analysed integral field MEGARA and long-slit OSIRIS optical spectroscopic data of HuBi 1, the inside-out PN. The combined capabilities of these two GTC instruments have allowed us to study the ionization structure of HuBi 1 in unprecedented detail and to determine the true chemical abundances of the recent ejecta in its innermost regions. Our main findings can be summarized as follows:

(i) The multiple shell structure of HuBi 1 is clearly dissected, with an inner shell associated with the recent ejecta, an outer shell, and additional emission mainly in the low-ionization [N II] and [S II] lines from an intermediate region. The inverted ionization structure of the inner shell of HuBi 1 is dramatically confirmed, with the emission in the He II λ4686 line encompassing that in the [O III] lines, which in addition surrounds that of the low-ionization [N II] and [S II] emission lines. The morphology of the intermediate region and its excitation are indicative of the interaction between the expanding ejecta of the inner shell and the old nebula. This intermediate region can be envisaged as the precursor of the petal-like structure clearly developed in the evolved born-again PNe A 30 and A 78.

(ii) The high-dispersion integral field spectroscopic data obtained with MEGARA have proven to be conclusive to separate for the first time the faint emission of the H Balmer lines from the inner shell from the bright emission of the outer shell. The emission in the Hβ and Hα lines from the inner shell of HuBi 1 have been accurately obtained, allowing us to compute reliable relative line intensity ratios to determine the spatially varying extinction and excitation, and to compute the true chemical abundances of the inner shell.

(iii) The extinction coefficient c(Hβ) of the inner shell ($\simeq$2.2) is on average twice that of the outer shell ($\simeq$1.1). The increased absorption towards the central regions of HuBi 1 is consistent with the idea that large amounts of dust have been recently produced there as suggested by the remarkable brightness reduction of its CSPN, IRAS 17514 − 1555, by $\sim$10 mag in the last 50 yr.

(iv) The improved relative line intensity ratios have allowed us to undoubtedly confirm that the inner shell is ionized by shocks using BPT diagrams. On the other hand, the outer shell is located on the photoionization zone of these diagram. Interestingly, the distributions of data points of the outer shell in the line ratio diagrams show a gradient, with points from the outermost regions clearly in the photoionization zone, but points from the innermost regions of the outer shell spatially consistent with the intermediate region described above being closer to the locus for shocks. This supports the idea that the intermediate region is partially shock-excited by the interaction of the recent ejecta with the old nebula.

(v) The total abundances by number considering shocks are in agreement with the chemical abundances obtained from CELs in the hydrogen-poor knots of other born-again PNe such as A 30, A 58, and A 78. This is also the case for the total abundances by mass computed assuming an ADF of 100 similar to other born-again PNe. In particular, the large amount of He complies the hydrogen-poor nature of the ejecta predicted in born-again scenarios. Our observation did not detect any carbon lines and we could not measure its abundances, but it can be expected that large amounts of carbon are to be trapped into C-rich dust. Moreover, some carbon and oxygen can be found forming CO molecules. It is suggested that the depletion of carbon and oxygen into dust grains and CO molecules can bring

the chemical abundances of the recent ejecta in HuBi 1 close to those of its [WC] CSPN.

ACKNOWLEDGEMENTS

BM-M and MAG are funded by the Spanish Ministerio de Ciencia, Innovación y Universidades (MCIU) grant PGC2018-102184-B-I00, co-funded by FEDER funds. BM-M, BP, MAG, and SC acknowledge support from the State Agency for Research of the Spanish MCIU through the 'Center of Excellence Severo Ochoa' award to the Instituto de Astrofísica de Andalucía (SEV-2017-0709). JAT is funded by UNAM DGAPA PAPIIT project IA100720 and the Marcos Moshinsky Fundation (Mexico).

This work has made used of observations made with the Gran Telescopio Canarias (GTC), installed at the Spanish Observatorio del Roque de los Muchachos of the Instituto de Astrofísica de Canarias, in the island of La Palma. This work made use of IRAF, distributed by the National Optical Astronomy Observatory, which is operated by the Association of Universities for Research in Astronomy under cooperative agreement with the National Science Foundation. This work has made extensive use of NASA's Astrophysics Data System. Based on observations made with the NASA/ESA Hubble Space Telescope, and obtained from the Hubble Legacy Archive, which is a collaboration between the Space Telescope Science Institute (STScI/NASA), the Space Telescope European Coordinating Facility (ST-ECF/ESA) and the Canadian Astronomy Data Centre (CADC/NRC/CSA).

DATA AVAILABILITY

The data underlying this article will be shared on reasonable request to the corresponding author.

REFERENCES

Allen M. G. et al., 2008, ApJS, 178, 20
Asplund M. et al., 2009, ARA&A, 47, 481
Baldwin J. A., Phillips M. M., Terlevich R., 1981, Publ. Astron. Soc. Pac., 93, 5
Balick B., Guerrero M. A., Ramos-Larios G., 2021, ApJ, 907, 104
Binette L., Dopita M. A., Tuohy I. R., 1985, ApJ, 297, 476
Clayton G. C. et al., 2013, ApJ, 771, 130
Cox D. P., 2005, ARA&A, 43, 337
Dopita M. A., 1976, ApJ, 209, 395
Dopita M. A., 1977, ApJS, 33, 437
Dopita M. A., 1978, ApJS, 37, 117
Dopita M. A. et al., 2018, MNRAS, 475, 424
Evans A. et al., 2020, MNRAS, 493, 1277
Filippenko A. V., 1982, Publ. Astron. Soc. Pac., 94, 715
Gil de Paz A., Carrasco E., Gallego J. et al., 2018, Proc. SPIE, 10702, 1070217
Guerrero M. A., Manchado A., 1996, ApJ, 472, 711
Guerrero M. A. et al., 2018, Nat. Astron., 2, 784
Howarth I. D., 1983, MNRAS, 203, 301
Hu J. Y., Bibo E. A., 1990, A&A, 234, 435
Iben I. et al., 1983, ApJ, 264, 605
Jacoby G. H., Ford H. C., 1983, ApJ, 266, 298
Kauffmann G., Heckman T. M., Tremonti C. et al., 2003, MNRAS, 346, 1055
Kewley L. J. et al., 2001, ApJ, 556, 121
Kewley L. J., Groves B., Kauffmann G. et al., 2006, MNRAS, 372, 961
Lau H. H. B., De Marco O., Liu X.-W., 2011, MNRAS, 410, 1870
Leuenhagen U., Hamann W.-R., 1998, A&A, 330, 265
Luridiana V., Morisset C., Shaw R. A., 2015, A&A, 573, A42
Manchado A., Pottasch S. R., Mampaso A., 1988, A&A, 191, 128
Miller Bertolami M. M., Althaus L. G., Serenelli A. M., Panei J. A., 2006, A&A, 449, 313
Morisset C., 2018, wtl..conf, 2, Available at:https://walk2018.weebly.com/
Osterbrock D. E., Ferland G. J., 2006, in Osterbrock D. E., Ferland G. J., eds, Astrophysics of gaseous nebulae and active galactic nuclei, 2nd. University Science Books, Sausalito, CA, p. 2006
Pascual S., Cardiel N., Gil de Paz A. et al., 2019, in Montesinos B., et al., eds, Highlights on Spanish Astrophysics X. Proc. XIII Scientific Meeting of the Spanish Astronomical Society. p. 227
Peña M., 2005, Rev. Mex. Astron. Astrofis., 41, 423
Peña M., Stasińska G., Medina S., 2001, A&A, 367, 983
Peña M., Hernández-Martínez L., Ruiz-Escobedo F., 2021, MNRAS, 503, 972
Perea-Calderón J. V., García-Hernández D. A., García-Lario P. et al., 2009, A&A, 495, L5
Pollacco D. L., Hill P. W., 1994, MNRAS, 267, 692
Raga A. C. et al., 2008, A&A, 489, 1141
Rechy-García J. S. et al., 2020, ApJ, 903, L4
Rechy-García J. S. et al., 2021, MNRAS, 508, 2254
Reindl N. et al., 2017, MNRAS, 464, L51
Rodríguez L. F. et al., 2017, Rev. Mex. Astron. Astrofis., 53, 45
Santamaría E. et al., 2020, ApJ, 892, 60
Schönberner D., 1979, A&A, 79, 108
Sutherland R. S., Dopita M. A., 2017, ApJS, 229, 34
Sutherland R. et al., 2018, Astrophysics Source Code Library, record ascl:1807.005
Tafoya D. et al., 2022, ApJ, 925, L48
Toalá J. A. et al., 2021a, MNRAS, 503, 1543
Toalá J. A. et al., 2021b, MNRAS, 505, 3883
Tody D., 1993, in J. Hanisch R., Brissenden R. J. V., Barnes J., eds, Astronomical Data Analysis Software and Systems II, Vol. 52, Astron. Soc. Pac., San Francisco, p. 173
Ueta T., Otsuka M., 2021, Publ. Astron. Soc. Pac., 133, 093002
Veilleux S., Osterbrock D. E., 1987, ApJS, 63, 295
Wesson R., Liu X.-W., Barlow M. J., 2003, MNRAS, 340, 253
Wesson R., Barlow M. J., Liu X.-W., Storey P. J., Ercolano B., De Marco O., 2008, MNRAS, 383, 1639
Wesson R., Jones D., García-Rojas J. et al., 2018, MNRAS, 480, 4589

APPENDIX A: SELECTION AND CORRECTION OF EMISSION LINES IN OSIRIS DATA

The emission of the inner shell of HuBi 1 is contaminated by that of the surrounding outer shell. This is a typical situation in multiple shell PNe where the contribution of the emission from the outer shell to the inner shell is normally ignored because the emission from the inner shell is much brighter than that of the outer shell. This is not the case for the emission from the inner shell of HuBi 1, for which the emission from some lines (e.g. the H Balmer lines) is much fainter than that from the outer shell. Therefore, the contribution of the emission from the outer shell to the inner shell cannot be ignored and the measurement of the emission line fluxes for the inner and outer shells of HuBi 1 require a tailored approach.

The OSIRIS data provide information on the spatial location of the emission and cannot be used to disentangle the fraction of the emission at the location of the inner shell that corresponds to the inner and outer shells. Fortunately, the kinematic information provided by the MEGARA data can be used to separate the emission of the inner shell from that of the outer shell given their different expansion velocities (Rechy-García et al. 2020). Accordingly, we have defined four different types of emission lines: purely internal, purely external, external with some inner emission, and internal with some external emission. The classification for each emission line detected in HuBi 1 is presented in Table A1 .

(i) Purely internal (PI) or external (PE) emission lines.

Table A1. Atmospheric differential chromatic refraction (DCR) shift for the emission lines detected in the GTC OSIRIS spectrum of HuBi 1 and line classification according to the fraction of emission from the inner and outer shells.

Line	DCR shift (arcsec)	Line classification
[O II] 3727	+1.22	IwE
[Ne III] 3869	+1.08	PI
Hζ+He I 3889	+1.06	PE
Hϵ+[Ne III] 3969	+0.99	–
He I 4026	–	PE
[S II] 4069	+0.91	PI
Hδ 4101	+0.88	PE
Hγ 4340	+0.71	PE
[O III] 4363	+0.70	PI
He I 4471	+0.63	PE
C I:O II:N II:4562+4570	+0.58	PI
He II 4686	+0.51	PI
Hβ 4861	+0.43	EwI
[O III] 4959	+0.38	PI
[O III] 5007	+0.36	PI
He I 5016	+0.36	PE
[N I] 5199	+0.29	IwE
[N II] 5755	+0.11	PI
He I 5876	+0.08	EwI
[O I] 6300	+0.01	PI
[S III] 6312	−0.01	PI
[O I] 6363	−0.02	PI
[N II] 6548	−0.05	IwE
Hα 6563	−0.05	EwI
[N II] 6584	−0.06	IwE
He I 6678	−0.07	PE
[S II] 6717	−0.08	IwE
[S II] 6731	−0.08	IwE
He I 7065	−0.13	PE
[Ar III] 7135	−0.14	PI
C II 7236	−0.16	PI
C I, O II? 7289	−0.16	PI
[O II] 7320	−0.17	PI
[O II] 7330	−0.17	PI
N I:O II 7379	−0.18	PI

Lines whose emission arises mostly from the inner or outer shell, such as the [O III] or He II and the He I lines, respectively. The fluxes are measured directly from the spectra extracted from the corresponding apertures overlaid on Fig. 1, i.e, the top and bottom spectra in Fig. 5, but for the emission lines with available GTC MEGARA images (e.g. the [O III], He II and He I emission lines), whose total integrated fluxes are computed from these images.

(ii) Lines mostly from the external shell with internal emission (EwI).

The emission of the outer shell is dominated by H Balmer and He I recombination lines, implying strong contamination to the emission of the inner shell in these lines. The different expansion velocity of the inner and outer shells and the tomographic capability of the GTC MEGARA data have allowed us to disentangle the emission in the Hα and Hβ lines as described in Sections 3.2.1 and 3.2.2. The flux of these emission lines from both shell is thus measured directly on the GTC MEGARA images of each shell. In the case of He I lines, with only GTC OSIRIS data, only 5875 He I line had enough S/N to obtain the emission of the inner shell by using lines profile. As well as in Hβ and Hα lines profiles has slight bumps at the location of inner shell corresponding with the emission of this shell, He I should has this bumps and we use Hβ to extract the inner emission of the He I line. First, the dereddened Hβ profile of inner shell (see, section 3.2.1) was subtracted from the total profile in order to obtain non-contaminated emission of the outer shell. Then the peaks of total emission He I profile and Hβ pure outer emission profile were equated to estimated the pure emission of He I line. Finally we subtract the Hβ profile from He I to obtain the emission purely internal of the later. Although this method is subject to a worse S/N, it provide an estimation of He I 5875 line. A similar method was also applied to other He I lines however the S/N was too large to obtain emission of the inner shell. Therefore, these lines were assumed to be PE.

(iii) Lines mostly from the internal shell with external emission (IwE).

A number of important emission lines are notably bright in the inner shell, but the outer shell still presents significant emission. In the case of the emission lines of [N I] and [O II], with only GTC OSIRIS data, the surface brightness of the outer shell (top panel Fig. 5) in these lines was measured and an average value adopted on the assumption that it is an homogeneous shell. Then, that emission was subtracted from the emission of the inner shell (bottom panel Fig. 5) considering an equivalent aperture for the inner shell to obtain its net flux. The flux for outer shell was computed scaling its average surface brightness to the yellow and red apertures in Fig. 1 to consider the flux of the outer shell projected on to the inner shell. In the case of the emission lines of [N II] and [S II], which have GTC MEGARA data, a similar procedure to that used for the Hα and Hβ lines could have been applied. However, the emissions from the inner and outer shells of [N II] and [S II] could not be perfectly separated in the velocity space, as was done for Hα and Hβ, because the emission from the inner shell is present in all velocity channels, not only in high-velocity components, whereas that of the outer shell has emission from an intermediate region occupying velocity channels with relatively high expansion velocities (Toalá et al. 2021b). In this case, we first determined the emission of these lines from the inner shell that could be isolated in high-velocity components as for Hα and Hβ. Then at lower velocities, where intermediate/outer and inner shells are present, a mask of 2.5 arcsec in radius was applied and the flux measured on this aperture. The flux of the inner shell was the sum of both terms, whereas for the outer shell, the flux adopted was that of the emission beyond 2.5 arcsec.

We note that the Hβ emission line is used to compute the different line ratios listed in Table 1. For the inner shell, these are computed using the total Hβ and line fluxes derived from the GTC MEGARA image if there is available GTC MEGARA image of the inner shell for that line. If there were no available GTC MEGARA image of that line, the Hβ flux is computed from a pseudo-slit on to the GTC MEGARA image at the location of the GTC OSIRIS slit (see next Appendix).

APPENDIX B: CORRECTING THE ATMOSPHERIC DIFFERENTIAL CHROMATIC REFRACTION IN THE OSIRIS DATA

The OSIRIS observations of HuBi 1 were obtained at the time around its culmination, but still at large airmass values at the ORM, in the range from 1.49 to 1.41, when notable differential chromatic refraction (DCR) effects can be expected. DCR effects are usually minimized selecting the position angle (PA) of the slit along the parallactic angle, which is close to the north–south direction near culmination. The PA of the slit during the observations was however

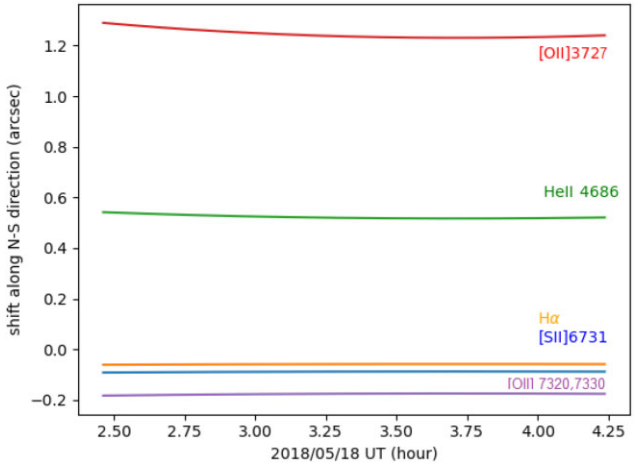

Figure B1. Variations of the shifts with respect to [N II] for different emission lines during the observations. DCR becomes noticeable in the blue zone of spectrum rising up 1.2 arcsec for [O II]λ3727. Due to the negligible variation, an average value of the shifted for each line can be adopted for the whole observation.

set almost orthogonally, at PA 90° along the east–west direction, to avoid background stars and to register nebular areas of the highest surface brightness, thus optimizing the scientific return of the observations. As a result, DCR effects cannot be ignored and need to be accounted for in the analysis of this data set.

According to Filippenko (1982), the positional shift along the parallactic angle caused by the DCR can be expressed in terms of λ and zenith distance z (or airmass m), which is a function of the observing time t. This shift is computed for a wavelength reference at 5000 Å adopting typical conditions of the ORM. We have computed the spatial shifts for the wavelength of each emission line of interest according to Filippenko's expressions, but referred them to the central wavelength of the Sloan *r'* filter at 6204 Å that was used for the acquisition of HuBi 1.

$$\mathrm{DCR}(\lambda) = R(\lambda) - R(\lambda_0) \approx 206265[n(\lambda) - n(\lambda_0)]\tan(z), \quad \text{(B1)}$$

$$n(\lambda)_{15,760} - 1 = \left[64.328 + \frac{29498.1}{146 - (1/\lambda)^2} + \frac{255.4}{41 - (1/\lambda)^2}\right], \quad \text{(B2)}$$

$$n(\lambda)_{T,P} - 1 = (n(\lambda)15, 760 - 1) \times \frac{P[1 + (1.049 - 0.0157T)10^{-6}P]}{720.883(1 + 0.003661T)}. \quad \text{(B3)}$$

The positional shift between emission lines at the blue and red extremes of the spectral range (for instance, the [O II] λ3727 and [O II] λλ7320, 7330 emission lines) was found to be larger than the slit width.

Since the parallactic angle is a function of time $pa(t)$ that varies quite rapidly near culmination, the shift of the slit along the orthogonal direction caused by DCR effects $s(t)$ needs to be corrected accordingly:

$$s(t) = DCR(\lambda, t) \times \cos\, pa(t). \quad \text{(B4)}$$

The variations of the shifts with respect to [N II] for different emission lines of interest such as [O II] λ3727, He II λ4686, Hβ, [O III] λ5007, [S II] λλ6716,6731, and [O II] λλ7320,7330 are shown in Fig. B1. This figure reveals that the variations of the shifts during the observations are not dramatic for the wavelength of each emission lines of interest.

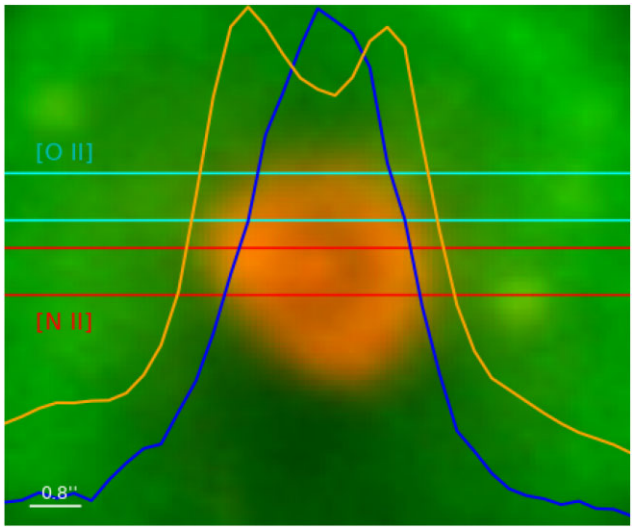

Figure B2. NOT ALFOSC [N II] λ6584 (red) and Hαλ6563 (green) colour composite picture of HuBi 1. Relative positions of OSIRIS slit for [O II] (cyan) and [N II] (red) are superimposed and also its corresponding lines profiles (blue) and (orange), respectively. The relative position of [O II] line falls just on the edge of the inner region, providing and single-peak profile, and not two as would be expected looking at Fig. 2, showing the DCR suffered by OSIRIS data set.

We can thus define slit positions for each emission line using median values of their shifts in Fig. B1 to characterize the spatial regions of HuBi 1 registered by these emission lines. A number of these equivalent slit positions are overlaid on an image of HuBi 1 in the [N II] λ6584 emission line in Fig. B2. The figure immediately reveals that different emission lines register different nebular regions. This is particularly significant for the small-sized inner shell of HuBi 1, implying that the comparison of spatial profiles and fluxes for different emission lines of this shell extracted from the OSIRIS 2D spectra has to consider these shifts (unlike the analysis presented by Peña et al. 2021).

In order to correct from these effects the intensity line ratio of a particular emission line to Hβ, we have adopted different strategies. For the inner shell, the intensity line ratio to Hβ of emission lines covered in the spectral range of the MEGARA data is derived from the whole emission of the inner shell, whereas that of emission lines only covered in the OSIRIS data are compared to the Hβ flux derived from the corresponding pseudo-slit of this line in the MEGARA data. For the outer shell, the MEGARA data do not cover the whole outer shell, thus the intensity line ratio to Hβ has been solely derived using the latter approach, i.e. the flux of the emission line is compared to the Hβ flux derived from the corresponding pseudo-slit of this line in the MEGARA data. This procedure warranties that the intensity line ratio to Hβ of a particular emission line is derived using line fluxes measured in the same nebular apertures for both emission lines.

APPENDIX C: MAPPINGS V SHOCK MODELS OF THE INNER SHELL OF HUBI 1

MAPPINGS V (see Sutherland & Dopita 2017) is able to produce line and continuum emissivity from shocked plasmas from non-equilibrium ionization objects, for example, radiative shocks in supernova remnants or shock structures surrounding Herbig-Haro objects. MAPPINGS V solves the coupled ionization and cooling equations in a time-dependent scheme. The first version of MAPPINGS

(see Binette, Dopita & Tuohy 1985) was developed as a result of a series of works presented by Dopita (1976, 1977, 1978). The code has been greatly improved since then and it now includes a detailed treatment of temperature-dependent collision strengths, new cooling functions, computations for optically thin plasmas and up to 80 000 cooling and recombination lines (see the historical improvement of the code presented in Sutherland & Dopita 2017).

Here we present in Tables C1–C4 the predicted line intensities of some of the models computed with MAPPINGS V following the methodology explained in Section 4.5 to estimate the chemical abundances of the inner shell of HuBi 1. All models are computed with a spectral resolution $R \approx 3000$, i.e. the line intensity ratios presented in Tables C1–C4 include the contribution of all emission lines computed in the model around the nominal wavelength that would be unresolved at this spectral resolution. We note that the expected contribution of contaminant emission lines is mostly negligible.

Tables C1 and C2 present emission line ratios referred to $I(\mathrm{H}\beta) = 100$ as they constrain the chemical abundances of helium, oxygen, and nitrogen with respect to hydrogen. The first five models in Table C1 were computed at fixed values of He/H and N/H to explore the variations of the emission line ratios with the O abundances. Then the O/H abundances ratio was fixed at its best value and the N/H abundances ratio varied in the next five columns. This table shows that high oxygen and nitrogen abundances are necessary to reproduce the emission lines of [O III] and [N II]. Once the best-fitting values of the O/H and N/H abundances ratios were determined, the He/H abundances ratio was varied in Table C2. Although the He I λ5876 emission line is not well reproduced by the adopted value of He/H, we note that different values of He/H lead to notable differences in the estimate of most emission lines (being clearly overestimated for $12 + \log(\mathrm{He/H}) > 13.0$).

Tables C3 and C4 explore the variations of the intensity line ratios of He, N, O, Ne, S, and Ar induced by changes of the physical conditions of the shock, namely the shock velocity v_s and the pre-shock density n_{pre}. We therefore preferred to refer the emission line ratios to $I([\mathrm{O\ III}]\ 5007) = 100$ to assess the relative changes in the line ratios from ions of those elements. It should be noted in Table C3 that the [O II] to [O III] line ratio peak at v_s of 100 km s^{-1}, then drops gradually at higher velocities. Indeed, the notable increase of the [O III] line intensities at velocities 140 km s^{-1} and above produces a sharp decline in most line ratios, particularly in the H I, He I, and He II recombination lines. Meanwhile the effects of the variations of the pre-shock density n_{pre} explored in Table C4 reveal notable changes in the intensity ratios of lines from low ionization species, such as He I, [O I], [O II], [N I], [N II], and [S II], with respect to [O III], whereas other higher ionization species show less dramatic variations.

This paper has been typeset from a TEX/LATEX file prepared by the author.

Table C1. MAPPINGS V models assessing the variation of the oxygen and nitrogen abundances for the inner shell of HuBi 1. The values of $v_s = 80\,\mathrm{km\,s^{-1}}$, $n_{pre} = 1\,\mathrm{cm^{-3}}$, $B = 1\,\mu$G, $12 + \log_{10}(\mathrm{He/H}) = 13.0$, and $\mathrm{H/H^+} = \mathrm{He/He^+} = 1$ have been fixed in all models. O/H stands for $12+\log_{10}$(O/H), N/H for $12+\log_{10}$(N/H), and RO3 denotes the ratio [O III] λ4363/[O III] λ5007.

Line	Obs.	N/H=7.9					O/H=9.8				
		O/H = 8.0	O/H = 9.0	O/H = 9.8	O/H = 10.0	O/H = 10.2	N/H = 7.9	N/H = 8.9	N/H = 9.9	N/H = 10.9	N/H = 11.9
[O II] 3727	8360	166.6	723.2	1049.7	978.6	985.3	1049.7	968.8	571.2	66.5	398.1
[Ne III] 3869	622	1.7	15.6	54.6	97.0	88.4	54.6	74.9	54.9	13.0	63.8
[S II] 4069	111	5.2	20.4	21.1	24.0	21.7	21.1	23.7	14.2	2.1	37.4
[O III] 4363	30.6	0.7	6.1	22.8	44.2	43.7	22.8	31.1	25.0	6.3	28.3
He II 4685	134	43.8	48.2	49.2	75.3	60.6	49.2	70.6	66.8	49.7	69.0
[O III] 4959	101	3.2	26.8	109.9	229.0	252.6	109.9	149.1	129.2	45.1	143.3
[O III] 5007	324	9.2	77.7	317.8	662.1	730.1	317.8	431.0	373.4	130.4	414.5
[N I] 5199	75.6	58.4	18.7	2.1	1.1	0.7	2.1	22.1	119.3	266.9	111.3
[N II] 5755	60.2	9.2	4.4	1.1	0.7	0.5	1.1	10.4	66.3	85.7	88.4
He I 5876	< 20.5	286.0	361.8	468.9	399.5	322.6	468.9	422.7	336.7	165.6	388.1
[O I] 6300	95.5	27.2	88.9	51.1	37.7	33.9	51.1	56.6	30.4	5.3	76.5
[S III] 6312	4.5	0.6	3.4	7.1	9.2	9.4	7.1	7.6	5.3	1.1	5.7
[O I] 6363	28.3	8.7	28.4	16.3	12.1	10.8	16.3	18.1	9.7	1.7	24.5
[N II] 6548	330	126.6	45.2	8.1	5.6	3.4	8.1	86.9	552.2	871.3	754.3
Hα	274.0	323.5	325.2	397.3	410.0	436.3	397.3	392.4	407.4	472.3	361.9
[N II] 6584	1390	372.6	132.9	24.0	16.4	10.0	24.0	255.6	1624.6	2563.6	2219.4
[S II] 6716	135	62.3	181.2	160.4	144.5	133.7	160.4	172.2	104.0	18.1	75.7
[S II] 6731	112	50.3	168.1	163.7	159.5	128.7	163.7	190.4	115.0	17.4	117.4
[Ar III] 7135	11.1	0.5	3.7	8.3	13.8	12.9	8.3	11.0	7.8	1.7	9.2
[O II] 7319	31.6	7.4	42.9	70.7	73.9	62.5	70.7	73.8	43.1	3.7	88.8
[O II] 7329	26.2	6.0	34.7	57.1	59.7	50.5	57.1	59.6	34.8	3.0	72.0
RO3	0.094	0.076	0.078	0.072	0.067	0.060	0.072	0.072	0.067	0.048	0.068

Table C2. MAPPINGS V models assessing the variation of the helium abundances in the inner shell of HuBi 1. The values of $v_s = 80$ km s^{-1}, $n_{pre} = 1\,\mathrm{cm^{-3}}$, $B = 1\,\mu$G, $12 + \log_{10}(\mathrm{O/H}) = 9.8$, $12 + \log_{10}(\mathrm{N/H}) = 9.9$, and $\mathrm{H/H^+} = \mathrm{He/He^+} = 1$ have been fixed in all models. He/H stands for $12+\log_{10}$(He/H) and RO3 denotes the ratio [O III] λ4363/[O III] λ5007.

Line	Obs.	He/H				
		12.2	12.9	13.0	13.1	13.2
[O II] 3727	8360.0	185.7	493.7	571.2	652.6	721.9
[Ne III] 3869	622.0	38.7	58.8	54.9	50.2	49.9
[S II] 4069	111	6.4	12.0	14.2	16.9	21.1
[O III] 4363	30.6	20.6	27.9	25.0	21.8	20.5
He II 4685	134.0	19.1	66.0	66.8	66.7	73.0
[O III] 4959	101.0	129.4	149.8	129.2	108.6	98.5
[O III] 5007	324.0	374.2	433.0	373.4	314.1	284.9
[N I] 5199	75.6	221.4	90.6	119.3	152.1	190.1
[N II] 5755	60.2	17.2	58.8	66.3	74.3	83.3
He I 5876	< 20.5	60.8	299.7	336.7	395.9	474.7
[O I] 6300	95.5	44.6	20.4	30.4	42.2	57.9
[S III] 6312	4.4	3.0	5.4	5.3	5.4	5.6
[O I] 6363	28.3	14.2	6.5	9.7	13.5	18.5
[N II] 6548	330	285.6	485.5	552.2	622.0	718.5
Hα	274.0	487.2	406.6	407.4	408.0	404.5
[N II] 6584	1390	840.3	1428.5	1624.6	1830.1	2114.2
[S II] 6716	135	101.7	87.0	104.0	119.7	137.3
[S II] 6731	112	72.8	92.8	115.0	136.3	164.4
[Ar III] 7135	11.1	5.3	8.2	7.8	7.3	7.4
[O II] 7319	31.6	6.3	35.0	43.1	51.7	62.5
[O II] 7329	26.2	5.1	28.3	34.8	41.8	50.4
RO3	0.094	0.055	0.065	0.067	0.070	0.072

Table C3. MAPPINGS V models assessing the variation of the shock velocity v_s. The values of $n_{pre} = 1$ cm^{-3}, $B = 1\,\mu$G, $12 + \log_{10}$(O/H) = 9.8, $12 + \log_{10}$(N/H) = 9.9, $12 + \log_{10}$(He/H) = 13.0, and H/H$^+$ = He/He$^+$ = 1 have been fixed in all models.

		v_s (km s^{-1})						
Line	Obs.	80	100	120	140	160	180	200
[O II] 3727	2580.2	153.0	495.2	219.4	50.5	22.6	13.6	9.0
[Ne III] 3869	192.0	14.7	10.1	13.5	6.5	7.0	6.8	6.5
[S II] 4069	34.3	3.8	6.0	3.6	0.8	0.4	0.4	0.3
[O III] 4363	9.4	6.7	6.5	7.8	2.6	3.5	4.0	4.1
He II 4685	41.4	17.9	13.2	17.7	1.2	1.5	2.5	3.4
Hβ	30.9	26.8	54.8	43.5	0.3	0.4	1.0	0.6
[O III] 4959	31.2	34.6	34.6	34.6	34.6	34.6	34.6	34.6
[O III] 5007	100.0	100.0	100.0	100.0	100.0	100.0	100.0	100.0
[N I] 5199	23.3	31.9	64.3	24.9	3.2	2.2	2.3	1.5
[N II] 5755	18.6	17.7	50.8	23.9	5.4	2.8	1.8	1.3
He I 5876	< 6.3	90.2	131.7	63.9	2.4	1.7	2.4	1.4
[O I] 6300	29.5	8.1	13.8	7.8	0.7	0.5	0.8	0.4
[S III] 6312	1.4	1.4	3.2	1.8	0.7	0.8	0.8	0.8
[O I] 6363	8.7	2.6	4.4	2.5	0.2	0.2	0.2	0.1
[N II] 6548	101.9	147.9	296.6	183.8	36.0	15.4	13.6	6.9
Hα	84.5	109.1	245.5	175.6	1.0	1.7	3.8	2.2
[N II] 6584	429.0	435.0	872.7	540.9	106.0	45.4	40.1	20.2
[S II] 6716	41.7	27.9	48.9	26.4	6.7	3.2	2.8	1.7
[S II] 6731	34.6	30.8	41.9	29.5	4.8	2.3	2.7	1.3
[Ar III] 7135	3.4	2.1	2.0	1.7	0.9	0.6	0.5	0.4
[O II] 7319	9.8	11.5	28.6	16.0	2.2	1.1	0.8	0.5
[O II] 7329	8.1	9.3	23.2	13.0	1.8	0.9	0.6	0.4

Table C4. MAPPINGS V models assessing the variation of the pre-shock density n_{pre}. The values of $v_s = 80$ km s^{-1}, $B = 1\,\mu$G, $12 + \log$ (O/H)=9.8, $12 + \log$ (N/H) = 9.9, $12 + \log$ (He/H) = 13.0, and H/H$^+$ = He/He$^+$ = 1 have been fixed in all models.

		n_{pre} (cm^{-3})			
Line	Obs.	0.1	1.0	10	100
[O II] 3727	2580.2	1104.2	153.0	693.9	98.7
[Ne III] 3869	192.0	11.5	14.7	12.6	17.0
[S II] 4069	34.3	9.8	3.8	13.6	21.7
[O III] 4363	9.4	6.3	6.7	6.3	7.7
He II 4685	41.4	13.2	17.9	11.6	15.9
Hβ	30.9	16.6	26.8	93.3	25.8
[O III] 4959	31.2	34.6	34.6	34.6	34.5
[O III] 5007	100.0	100.0	100.0	100.0	100.0
[N I] 5199	23.3	45.4	31.9	124.1	20.6
[N II] 5755	18.6	100.2	17.7	72.7	40.7
He I 5876	< 6.3	47.0	90.2	444.8	107.6
[O I] 6300	29.5	10.0	8.1	32.0	44.6
[S III] 6312	1.4	6.1	1.4	3.9	1.8
[O I] 6363	8.7	3.2	2.6	10.2	14.3
[N II] 6548	101.9	611.1	147.9	461.8	199.4
Hα	84.5	68.7	109.1	371.2	84.8
[N II] 6584	429.0	1797.9	435.0	1358.7	586.6
[S II] 6716	41.7	87.4	27.9	79.7	13.7
[S II] 6731	34.6	62.1	30.8	68.2	18.0
[Ar III] 7135	3.4	2.2	2.1	2.4	2.6
[O II] 7319	9.8	54.8	11.5	46.2	37.1
[O II] 7329	8.1	44.4	9.3	37.4	30.1